Optimizing and Modeling Phase-Locked Deep Brain Stimulation to Suppress Tremor

Candidate #1002072
Supervisor: Professor Rafal Bogacz
MSc Neuroscience Dissertation, Hilary Term
13 April 2016

Word Count: 10355 words

Abstract

Deep brain stimulation (DBS) effectively suppresses tremors in essential tremor, dystonic tremor, and Parkinson's disease patients when administered as continuous, high-frequency stimulation in the thalamus. However, adverse effects of such nearly constant stimulation, which include speech and motor impairment and high power consumption, motivate the search for smarter, more energy-efficient DBS strategies. This dissertation aims to investigate one such strategy based on recent research, which suggests that tremor suppression in essential tremor patients may depend on the phase of tremor at which low-frequency stimulation is delivered (Cagnan et al., 2013).

The work presented in this dissertation attempts to demonstrate an optimal, phase-locked stimulation strategy that maximally suppresses the tremor of a single essential tremor patient. It also uses and extends the Kuramoto neural oscillator model (Kuramoto, 1984; Tass, 2003; Wilson and Moehlis, 2014) to show the limitations such a mathematical model has in explaining an optimal, phasic stimulation strategy that is consistent with the one demonstrated in the clinical setting.

Two additional contributions are outlined in this dissertation: First, building off the Rayleigh test (Mardia, 1975), a novel, parameterized circular statistic to test weighted circular uniformity is described and analysed. Second, a web simulation of the proposed oscillator model is presented as both a research tool and a public engagement resource.

Table of Contents

Table of Figures

Table of Tables

Table of Equations

Introduction

Tremors are a common, debilitating symptom of several motor disorders. Continuous, high-frequency deep brain stimulation (DBS) in the thalamus has been a highly effective treatment for suppressing tremors in patients with Parkinson's disease, essential tremor, and dystonic tremor (Benabid et al., 1991). However, DBS also disrupts physiological motor function (Chen et al., 2006; Ray et al., 2009) and can cause adverse effects like speech impairments and gait instability (Zhang et al., 2010; Baizabal-Carvallo et al., 2014). The continuous, energy-consuming nature of conventional DBS has an additional toll in requiring the replacement of DBS implant batteries every few years. Together, these effects motivate research for a more efficient DBS paradigm that reaps the same tremor-suppressing benefits of typical DBS yet stimulate the thalamus sparingly and smartly.

While conventional DBS has some parameters, such as the strength and frequency of stimulation, that can be optimally tuned, typical, continuous, high-frequency stimulation does not change once parameters are set. Recently, a closed-loop paradigm known as adaptive DBS (aDBS) only administers stimulation when a threshold level of beta oscillations – neurons firing within the beta frequency range of 13-30Hz – in the basal-ganglia is exceeded (Little and Brown, 2012; Little et al., 2013, 2015; Rosa et al., 2015). High levels of beta oscillations in the basal-ganglia cortical loop have been linked to Parkinsonian symptoms such as limb rigidity and bradykinesia, a condition of slowness of movement, yet they have not been associated with tremor (Hammond et al., 2007). Thus, current aDBS paradigms are limited to treating non-tremor, Parkinsonian-specific symptoms.

Recent work suggests the potential for an alternative, tremor-suppressing aDBS paradigm by timing stimulation to a specific phase of tremor, that is, a particular point in a tremor oscillation. This research shows a tremor-suppressing effect when the phase of low-frequency DBS becomes synchronized with the phase of hand tremor in tremulous essential tremor (Cagnan et al., 2013) and Parkinson's disease patients (Azodi-Avval and Gharabaghi, 2015). In such patients, tremor oscillations occur at around 4-6 Hz, which is also the characteristic oscillation frequency in certain basal ganglia regions of tremulous patients (Hirschmann et al., 2013). It has been shown that thalamic neural activity synchronized to tremor frequency drives the automatic, repetitive movement (Hua, 2004). Thus, it may be plausible that stimulating the thalamus according to tremor phase may desynchronize the neural activity responsible for tremulous behavior (Beudel and Brown, 2015).

A computational model (Tass, 2003) describes how DBS can be incorporated into a common neural oscillator model, the Kuramoto model (Kuramoto, 1984), to simulate the synchrony of thalamic neurons and the desynchronizing effect of DBS. A recent work proposes an optimal, close-looped DBS strategy that depends on the phase of an individual neuronal oscillator (Wilson and Moehlis, 2014). However, this computational research has not been used to determine an optimal, adaptive DBS strategy based on the phase of tremor.

This dissertation uses tremor data collected from an experimental trial that times the administration of short, 35ms bursts of high-frequency DBS to a specific tremor phase of an essential tremor patient throughout a duration of 5 seconds (Cagnan and Brown, 2016). Using this experimental tremor data, this dissertation demonstrates that tremor phase-locked DBS yields a statistically significant, phase-dependent change in tremor amplitude and identifies an optimal range of tremor phases at which phase-locked DBS best suppresses tremor for this patient. This work also presents several extensions to the Kuramoto model and tests the extent to which the model can explain the clinical, phase-dependent tremor suppression observed in the essential tremor patient.

In summary, it is hoped that this work will serve as a stepping stone towards further research in developing not only a closed-loop, tremor phase-locked DBS paradigm but also a biologically-plausible model to explain how such stimulation effectively dampens tremor.

Methods

Experimental data collection was conducted by Dr. Hayriye Cagnan (Cagnan and Brown, 2016), and the optimization of model parameters was done by Dr. Gihan Weerasinghe. All other methods described in this section were designed and carried out by the author.

Experimental Data Collection

The experimental data analyzed in this dissertation was collected with the approval of the appropriate, local ethics committee and with the informed consent of all patients (Cagnan and Brown, 2016).

One essential tremor patient had four DBS electrodes inserted into their left ventralateral thalamus; placement of electrodes was confirmed using CT and MRI imaging after the operation. An accelerometer with three axes was attached to the index finger of the patient's right hand. Minimal, online processing was conducted on the accelerator axis with the most tremor. With a sampling rate of 10,417 Hz, this slightly processed signal from the dominant tremor axis is used and analyzed throughout this dissertation.

The tremors of the essential tremor patient were recorded when phase-locked, 35ms bursts of 130Hz DBS were administered throughout a 5-second block (Figure 1). Stimulation was phase-locked to tremor, which was measured by the hand-mounted accelerometer. Given a phase θ for a block, whenever the tremor oscillation passed phase θ, a 35ms burst of 130Hz DBS was administered (Figure 3). 9 blocks were recorded for each of the following 12 phases: 0°, 30°, 60°, 90°, 120°, 150°, 180°, 210°, 240°, 270°, 300°, 330° (with the exception of the 180° phase, for which only 8 blocks were successfully recorded). There was at least 1 second of no stimulation between blocks.

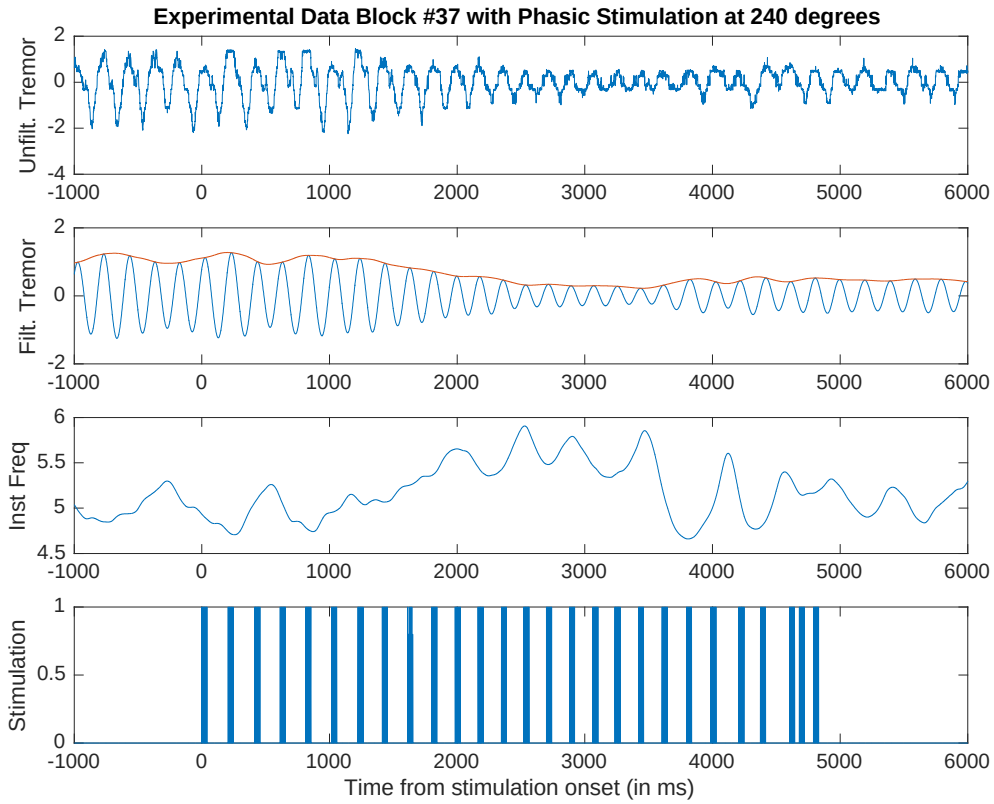

Figure 1: An Experimental Block with Phasic Stimulation at phase 240°

(1st row) The unfiltered tremor acceleration signal (m/s^2) was recorded by a single hand-mounted accelerometer. (2nd row) The tremor signal from the 1st row was band-pass filtered between 3Hz and 6Hz; the tremor amplitude (m/s^2) is traced in orange and was derived from the analytical signal. (3rd row) The instantaneous frequency (Hz) of the tremor amplitude was also derived from the analytical signal. (4th row) 35 ms bursts of 130 Hz, phase-locked stimulation were applied whenever the tremor amplitude passed the 240° phase.

Tremors were recorded in 9 batches (Figure 2). In each batch, 12 blocks were recorded, one for each of the 12 phases. To mitigate the effect a particular order of phasic stimulation blocks may have, the order of phase blocks was randomly permuted for each batch.

In between batches, the patient rested their hands from the extended, elevated hand position maintained during the batches, resulting in negligible tremor amplitude being recorded (Figure 2, see filtered amplitude signal during t = 1000-1200 seconds). These rest periods explain the noisy instantaneous frequency calculated in between batches.

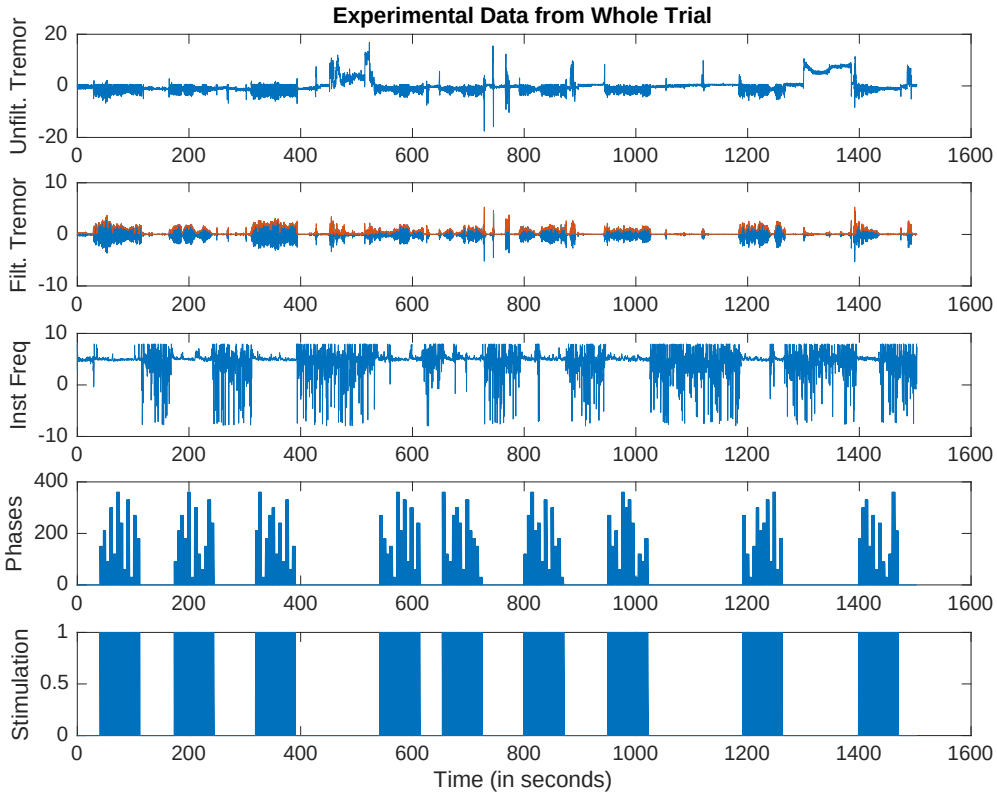

Figure 2: Experimental Data for Whole Trial

(1st row) The unfiltered tremor signal (m/s^2) was recorded by a single hand-mounted accelerometer. (2nd row) The unfiltered tremor signal was band-pass filtered between 3Hz and 6Hz; the tremor amplitude is traced in orange. (3rd row) The instantaneous frequency (Hz) of the filtered tremor amplitude was derived. (4th row) The phase (degrees) of stimulation was set *a priori* via a random permutation for each batch. (5th row) 35 ms bursts of 130 Hz, phase-locked stimulation were applied whenever the tremor amplitude passed the phase for a given block; phase of tremor was calculated online throughout the trial from the filtered amplitude.

During the experiment, to calculate the phase of the tremor, the signal from the dominant tremor axis of the unfiltered tremor was band-pass filtered online to $\pm$2Hz around the tremor frequency. Then, the tremor cycle's phase was estimated from the tremor frequency and the previous cycle's zero crossing of the online, filtered signal. When the target phase was detected from the online, filtered signal, DBS is administered at 130 Hz for 35 milliseconds; this corresponds to the delivery of 6 pulses (Figure 3). Because the filtered signal was calculated online, it was shifted in time and resulted in a phase shift. This shift was corrected for in the subsequent data processing and analysis as well as all presented figures.

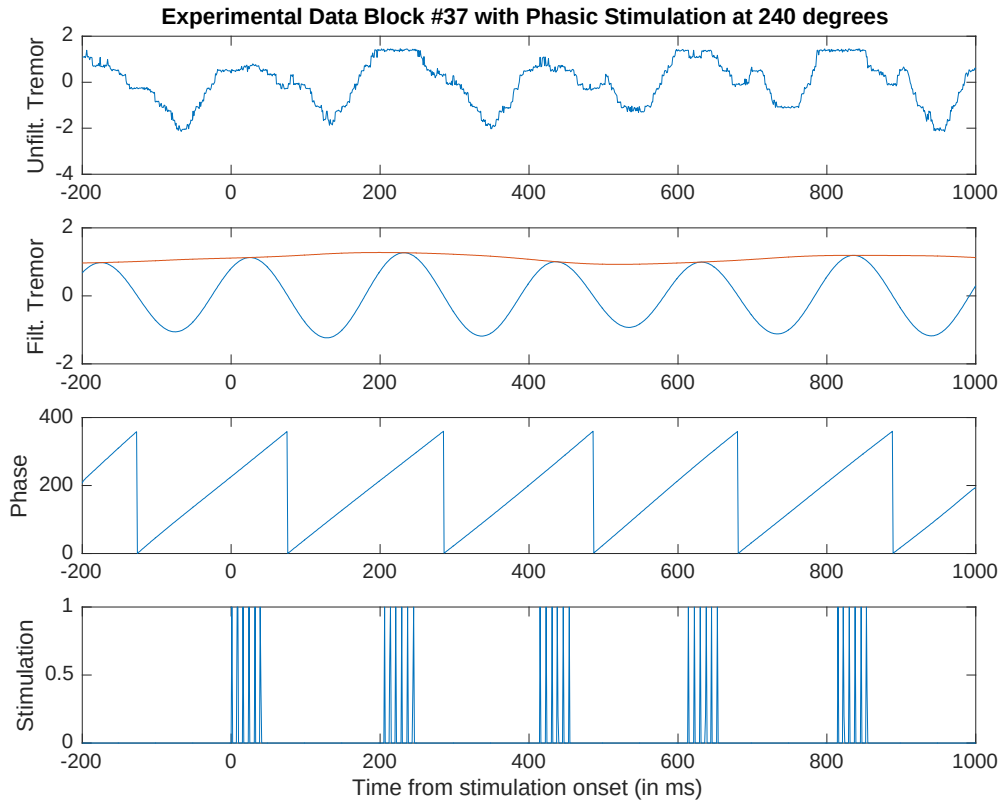

Figure 3: First second of an Experimental Block with Phase-locked Stimulation at 240°

(1st row) The unfiltered tremor signal (m/s²) was recorded by a single hand-mounted accelerometer. (2nd row) The unfiltered tremor signal was band-pass filtered between 3Hz and 6Hz; the tremor amplitude (m/s²) is traced in orange. (3rd row) The phase (degrees) of the tremor was calculated online from the filtered tremor throughout the whole trial. (4th row) A 35 ms burst of 130 Hz stimulation, resulting in 6 pulses, was applied every time the tremor amplitude passed phase 240°.

Experimental Data Processing

All data processing and analysis was conducted using custom MATLAB code.

The tremor signal, with an original sampling rate 10,417 Hz, was resampled at 1000 Hz. The resampled signal was then band-pass filtered between 3 Hz and 6 Hz using the second-order Butterworth filter (Butterworth, 1930). The resampled and filtered signal is used in all analyses unless otherwise mentioned.

The tremor amplitude (Equation 2) was calculated by taking the complex magnitude of the analytic signal (Equation 1) of the filtered tremor signal.

$$A(t) = f(t) + iH[f(t)]$$

Equation 1: Analytic Signal of Filtered Tremor Signal

The analytical signal of the tremor consists of the original signal of the filtered tremor, $f(t)$, and the Hilbert transform of the original signal, $H[f(t)]$.

$$a(t) = \sqrt{f(t)^2 + H[f(t)]^2}$$

Equation 2: Tremor Amplitude from Analytical Signal (Equation 1)

The instantaneous frequency was calculated by smoothing the derivative of the filtered tremor signal. First, the difference between each 1 millisecond time step of the tremor amplitude was calculated; this difference vector was then smoothed. Finally, the instantaneous frequency, $f(t)$, was calculated by scaling the smoothed difference vector, $d(t)$, by the sampling rate, r = 1000 Hz, and by $1/(2\pi)$ to reflect the derivative of the filtered tremor signal (Equation 3).

$$f(t) = \frac{rd(t)}{2\pi}$$

Equation 3: Instantaneous Frequency

The frequency of a time period can also be calculated by counting the number of zero crossings of the filtered tremor signal. The results reported in this work use instantaneous frequency; however, some additional results included in Appendix 1 used frequency calculated via the zero-crossings method. Qualitatively, results obtained using the two different methods for calculating frequency were similar.

Experimental Data Analysis

For each block, measures of the change in tremor amplitude, frequency, and phase respectively were calculated in order to analyze the effects of phase-locked DBS. The main metrics are described below; however, additional metrics were developed and are included in Appendix 1.

Calculating Change in Amplitude and in Frequency

The same metric was used to calculate change in amplitude and change in frequency (Equation 4). Let $\tilde{g}_a(x, y)$, where $x, y \in [-1,5]$ seconds, denote the median of the tremor amplitude between $t = x$ seconds and $t = y$ seconds in a block. Correspondingly, let $\tilde{g}_f(x, y)$ denote the median of the instantaneous frequency. Then, for a given 5 second block, the difference between the median of the amplitude (or instantaneous frequency) of the last second of the block, $\tilde{g}_m(4,5)$, and that of the preceding one second period of no stimulation, $\tilde{g}_m(-1,0)$, was calculated, where $m \in \{a, f\}$ denote amplitude or instantaneous frequency.

$$\Delta m = \tilde{g}_m(4,5) - \tilde{g}_m(-1,0)$$

Equation 4: Metric for Change in Amplitude and in Frequency

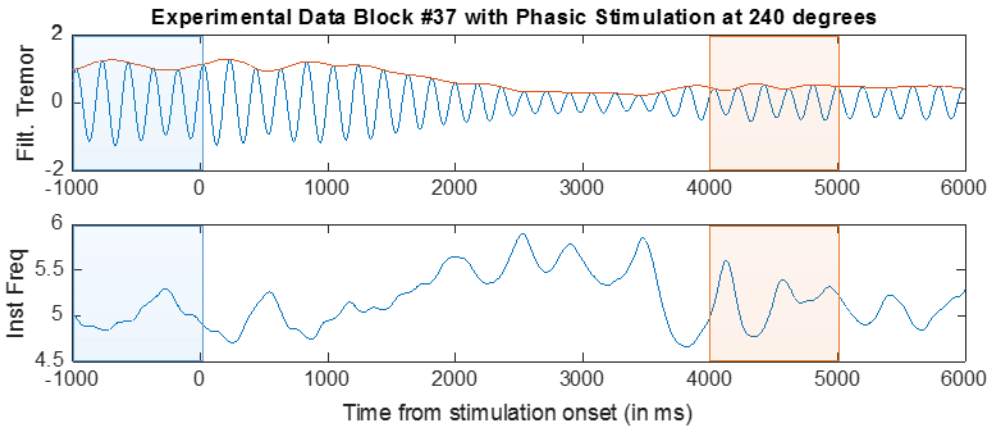

Figure 4: Epochs Used to Calculate Metric for Change in Amplitude and Frequency

The medians of the filtered amplitude (1st row, in orange) and of the instantaneous frequency (2nd row) from 4s-5s of a block (epoch bounded in orange) and are compared to that from -1s to 0s (epoch bounded in blue), during which there is no stimulation to compute change in amplitude and in frequency.

For change in amplitude and frequency, this metric was calculated for each of the 107 blocks and plotted in Figure 10, 1st and 2nd rows, with the median of each phase plotted as well.

Calculating the Phase Response Curve (PRC)

Let $\tilde{g}_f(x, y)$ be the median function $\tilde{g}$ defined in the previous section for instantaneous frequency. To calculate the change in phase, a reference frequency, f_r, was calculated by taking the median instantaneous frequency of the preceding one second period of no stimulation, i.e. $f_r = \tilde{g}_f(-1,0)$. Then, for $t = 0$ seconds to $t = 5$ of a given experimental block, the unwrapped phase, $\theta_a(t)$, in radians, of the filtered tremor signal, $f(t)$, was calculated.

$$\theta_a(t) = \text{unwrap}[\text{atan2}(\frac{H[f(t)]}{f(t)})]$$

Equation 5: Actual, Unwrapped Phase of Experimental Block

From Equation 1, $H[f(t)]$ is the imaginary component of the analytic signal, computing using the Hilbert transform, of the filtered tremor signal, $f(t)$. The MATLAB unwrap function corrects for phase jumps by adding 360° when phase jumps from 359° to 0°. The MATLAB atan2 function was used instead of inverse tan function, $\tan^{-1}$, in order to handle discontinuities at 90° and at 270°.

Then, accounting for the starting phase of the block, $\theta_a(0)$, in radians, the reference unwrapped phase was calculated by projecting the reference frequency (Equation 6).

$$\theta_r(t) = \theta_a(0) + 2\pi t f_r$$

Equation 6: Reference, Unwrapped Phase of Experimental Block

The equation for reference phase (Equation 6) corresponds to the first-order Taylor approximation around the neighborhood of $t = 0$ of the actual, unwrapped phase (Equation 7). This is because the derivative of phase is instantaneous frequency scaled by 2π, as one complete oscillation cycle is equivalent to travelling 2π or 360°. Thus, $\theta_a{}'(0)$ is approximated by $2\pi f_r$.

$$P_1(t) = \theta_a(0) + \theta_a{}'(0)t$$

Equation 7: 1st-Order Taylor Approximation of Phase Around $t = 0$

This first-order approximation sufficed, as the second derivative of phase was nearly always 0; thus, further order approximations (Equation 8) did not significantly differ from the first-order approximation.

$$P_k(t) = \sum_{i=0}^{k} \left(\frac{\theta_a^{(i)}(0)}{i!} t^i\right)$$

Equation 8: kth-Order Taylor Approximation of Phase Around $t = 0$

The time-evolution of the actual phase can also be approximated using a first-order Taylor expansion, which uses a different frequency, f_a, that reflects the actual frequency as a result of the current block's phase-locked stimulation (Equation 9).

$$\theta_a(t) \approx \theta_a(0) + 2\pi t f_a$$

Equation 9: 1st-Order Taylor Approximation of Actual, Unwrapped Phase of Experimental Block

Then, after solving for f_a in the equation for the approximation of $\theta_a(5)$ (Equation 10), which corresponds to the frequency at the end of the 5-second phase-locked stimulation block, the metric for change in phase can be calculated as the difference in degrees between the actual frequency and reference frequency (Equation 11a). Note that the approximation of f_a is the unwrapped phase of the block normalized by time, i.e. 5 seconds, and the length of a cycle, i.e 2π (Equation 10).

$$f_a \approx \frac{\theta_a(5) - \theta_a(0)}{2\pi(5)}$$

Equation 10: Approximation of Frequency as a Result of 5-second Phase-Lock Stimulation

$$\Delta\theta = 360°(f_a - f_r)$$

$$\Delta\theta = (360°)\frac{\theta_a(5) - \theta_r(5)}{10\pi}$$

$$\approx (360°)\frac{\theta_a(0) + 2\pi(5)f_a - (\theta_a(0) + 2\pi(5)f_r)}{10\pi} = 360°(f_a - f_r)$$

Equation 11a-b: Metric for Change in Phase

Alternatively, the metric for change in phase can be calculated as the difference in degrees between the unwrapped actual phase and unwrapped reference phase (Equation 11b, Figure 5).

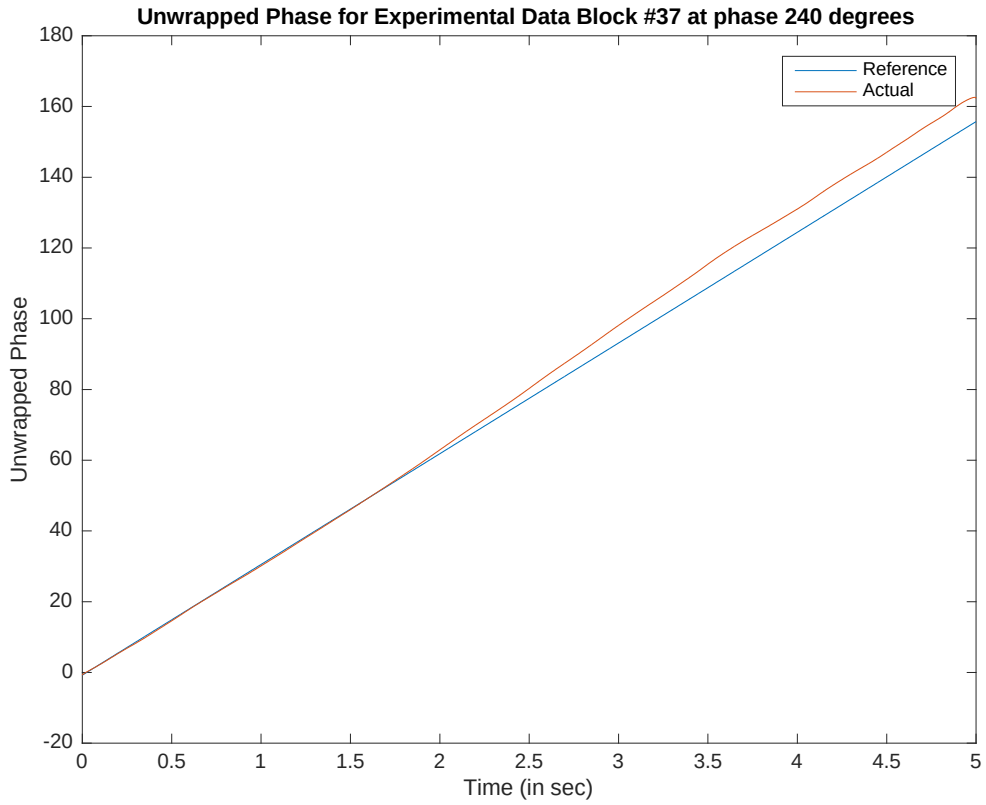

Figure 5: Unwrapped Phase of the Tremor Amplitude for an Experimental Block

The actual and real unwrapped phases (θ_a and θ_r respectively, in radians) are plotted for an experimental block in which 240° phase-locked stimulation was administered. The difference between the actual and real unwrapped phases at t = 5 seconds was used to calculate the change in phase (Equation 11).

For change in phase, this metric was calculated for each of the 107 blocks and plotted in Figure 10, 3rd row, with the median of each phase plotted as well.

Similarity between Change in Frequency and Change in Phase

Note that the change in phase metric is simply another way to calculate change in frequency. Both use the same reference frequency, $f_r = \tilde{g}_f(-1,0)$, that is the median, instantaneous frequency of the second preceding the block in which no DBS was administered. The only differences between the metrics are their units – change in frequency is given in Hz while change in phase is given in degrees – and the way they compute the "actual" frequency as a result of phase-locked DBS for a given block. The change in frequency metric approximates the "actual" frequency by

computing the median, instantaneous frequency of the last second of a given block, i.e. $\tilde{g}_f(4,5)$ (Equation 4), while the change in phase metric approximates the "actual" frequency using the unwrapped phase of a given block (Equation 10). Table 2 shows the strong correlation strength between the change in frequency and change in phase metrics. Thus, the two metrics are approximations of the same measure.

Significance Testing using Circular Statistics

In order to test whether there was a significant effect in the change in amplitude, frequency, and phase, circular statistics tests were used. In this section, an explanation of the relevant statistics – including the presentation of a novel, weighted, parametric circular test – will first be presented, followed by a description of how they were used to test significance in the experimental data.

Rayleigh Statistic

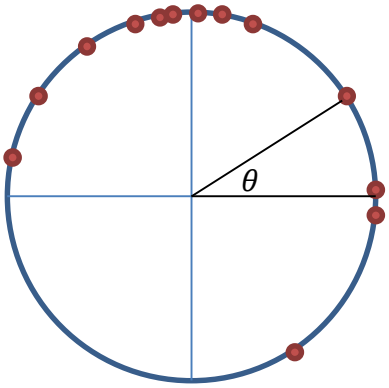

Figure 6: Example Phases Plotted Along Unit Circle

The Rayleigh circular statistic, z_r, is a non-parametric metric used to test whether a set of phases is significantly non-uniform (Mardia, 1975). The Rayleigh statistic computes the mean vector of all phases plotted along the unit circle (Figure 6), where R is the result vector's magnitude and (X, Y) is its Cartesian coordinate; the statistic z_r is the square of the radius, R, scaled by the number of phases, N (Equation 12). This statistic fails on equally spaced out n-modal data, such as diametrically bimodal data with clusters at 0° and 180° or trimodal data with clusters at 0°, 120°, or 240°, as the equally-spaced clusters would cancel each other out.

$$X = \frac{1}{N}\sum_{n=1}^{N}\cos\theta_n \,, Y = \frac{1}{N}\sum_{n=1}^{N}\sin\theta_n$$
$$R^2 = X^2 + Y^2$$
$$z_r = NR^2$$

Equation 12a-c: Rayleigh Statistic

A computed Rayleigh statistic can then be compared against a p-value table indexed by the number of elements, *N* (Zar, 2010). Alternatively, a null distribution can be generated by repeatedly uniformly sampling *N* phases to form a set of phases and computing the Rayleigh statistic on such randomly generated sets. Then, an empirical cumulative distribution function (CDF) can be computed on the null distribution by simply ordering its Rayleigh statistics and a threshold *z* value can be found for a particular p-value. This is the procedure by which the standard p-value table for the Rayleigh statistic was generated (Zar, 2010).

Moore-Rayleigh Statistic

However, the Rayleigh statistic fails to weight phases. Because the phases are plotted along the unit circle, they all assume a radius or weight of 1. In order to test the significance of the change in amplitude, frequency, and phase of experimental data, a weighted circular statistic is required, where the radius of each data point corresponds to one of the above metrics and its phase is that data point's corresponding phase (Figure 7).

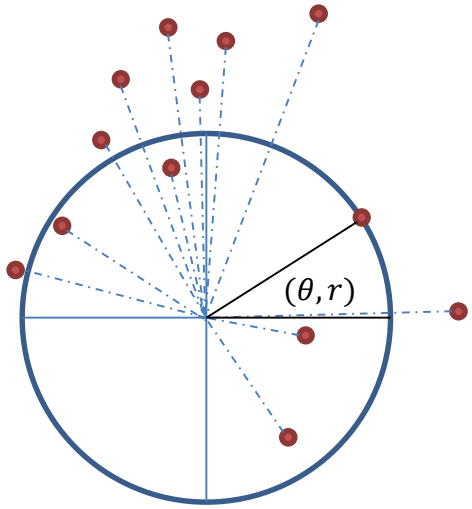

Figure 7: Example Phases with Different Radii or Weights

A non-parametric extension of the Rayleigh statistic, the Moore-Rayleigh statistic, z_m, weights phases by the rank order of their radii (Moore, 1980). Given a set of polar coordinates, $\{(\theta_n, r_n) \mid n = 1 \dots N\}$, the phases are reordered in ascending order by their radii: $(\theta_{(1)}, \theta_{(2)}, \dots, \theta_{(N)})$. Then, the Moore-Rayleigh test uses only the ordered phases to weight them by their rank-order when calculating the resultant vector. This results in the phase of the largest radius getting a weight of *N* while the phase of the smallest radius gets a weight of 1. Finally, the resultant vector's radius is then scaled by the inverse of the 1.5 power of the size of the set, *N* (Equation 13).

$$X = \sum_{n=1}^{N} n \cos \theta_{(n)}, Y = \sum_{n=1}^{N} n \sin \theta_{(n)}$$
$$R^2 = X^2 + Y^2$$

$$Z = \frac{R}{N^{3/2}}$$

Equation 13a-c: Moore-Rayleigh Statistic

Similar to the Rayleigh statistic, a computed Moore-Rayleigh statistic can then be compared against a standard p-value table indexed by the number of elements, N (Moore, 1980). The standard p-value table for the Moore-Rayleigh statistic was generated with a similar procedure as that for the Rayleigh statistic, by uniformly sampling phases and radiuses to generate a null distribution. Alternatively, a permutation test can be used to generate the null distribution by repeatedly shuffling the order of the dataset's phases and computing the Moore-Rayleigh statistic on each permutation. Then, an empirical CDF of the null distribution can be used to find threshold z values for p-values.

Scaled Rayleigh Statistic

In the process of conducting the research described in this work, a parametric, scaled Rayleigh statistic, z_s, was derived. To the best of the author's knowledge, this is the first parametric, weighted circular test based on the Rayleigh statistic.

The scaled Rayleigh test weights each phase θ_n by a corresponding radius r_n when calculating the resultant vector; the square of the result vector's radius is then scaled by the inverse of the size of the set, N (Equation 14).

$$X = \sum_{n=1}^{N} r_n \cos\theta_n \, , Y = \sum_{n=1}^{N} r_n \sin\theta_n$$

$$R^2 = X^2 + Y^2$$

$$z_s = \frac{R^2}{N}$$

Equation 14a-c: Scaled Rayleigh Statistic

Because the set of phases is parameterized by corresponding radii, a permutation test is the most appropriate test to compute p-values. A null distribution can be generated by repeatedly shuffling the set of N phases, randomly pairing them with a shuffled set of the N radii, and computing the scaled Rayleigh statistic on shuffled sets. Then, threshold z values can be found for p-values from the empirical CDF of the scaled Rayleigh statistics of the null distribution.

Alternatively, a null distribution could be generated by sampling from well-known statistical distributions, such as the uniform distribution for phases and the Normal distribution for radii, but moment parameters such as mean and variance would need to be fit to the dataset's radii in order for the null distribution's sampled radii to be reasonable. This dependency on the dataset makes the scaled Rayleigh statistic parametric.

Comparison of Weighted, Circular Statistics

Historically, non-parametric tests were preferable because a standard p-value table could be computed and used without regard to the specific dataset being tested. Given that computing power was much more limited just a few decades ago, eliminating the need to generate a null distribution was highly appealing. This was the motivation behind the development of the non-parametric Moore-Raleigh test. However, generating a null distribution today is now a negligible concern on most modern computers. Thus, more precise and powerful tests are now more preferable than ones that historically required less computational power.

In contrast to the Moore-Rayleigh test, the scaled Rayleigh test proportionally weights data points by the magnitude of their radii. The Moore-Rayleigh test can inaccurately suggest a significant effect in a dataset, when the differences among the dataset's radii are negligibly small yet are not captured in the non-parametric statistic. In this case, the dataset's phases are scaled by the rank order of their corresponding radii, which do not accurately reflect the magnitude of the radii and thus arguably leads to an inaccurate weighting.

Depending on the dataset, exactly what kind of effect is being tested, and whether diametric phases are related to each other, radii may or may not want to be restricted to the set of positive real numbers for the scaled Rayleigh test.

Further analysis on the strengths and limitations of the proposed scaled Rayleigh test was outside the scope of this project but may be an interesting and promising direction for future work.

The primary MATLAB resource for circular statistics did not include weighted circular statistics tests (Berens, 2012). The MATLAB implementations of the Moore-Rayleigh statistic and the scaled Rayleigh statistic used in this work were optimized and made available for public use (1002072, 2016a).

Significance Testing in Change of Amplitude, Frequency, and Phase

For $n \in \{1, \dots, N\}$, where $N = 107$ blocks, let θ_n denote the phase at which phase-locked stimulation was administered during the n-th experimental block and let $\Delta a_n, \Delta f_n$, and $\Delta\theta_n$ denote the respective change in amplitude, in frequency, and in phase metrics for the n-th block. Then, for each metric, both the Moore-Rayleigh statistic and the scaled Rayleigh statistic were computed, where z-scores (Equation 15) of the metric values, i.e. $\{\Delta m_n | \, n = 1, \dots, N\}$, where $m \in \{a, f, \theta\}$, were used as radii for the weighted tests. Permutation tests as described above were used to generate null distributions against which threshold z values and p-values could be evaluated.

$$z = \frac{x - \mu}{\sigma}$$

Equation 15: Z-Score

For the scaled Rayleigh test, both radii that include negative values and radii shifted so that all radii are positive were used. There was no palpable difference in results, so the significance tests reported in the Results section (Figure 11, Table 1) and in Appendix 1 directly use metric values, some of which are negative, as radii.

Kuramoto Model

A population of neurons can be represented as a set of oscillators. The Kuramoto model (Kuramoto, 1984) is one such neuronal oscillator model and has been extended to capture the effects of deep brain stimulation on highly synchronized thalamic neuronal populations, like those of essential tremor and Parkinson's disease patients (Tass, 2003). In this section, the model will first be explained; subsequently, the use of the model in this project will be outlined.

Tass' Kuramoto model captures four neuronal qualities – that they fire 1. regularly, 2. synchronously, 3. noisily, and 4. responsibly (to DBS). Let θ_i denote the phase of the i-th oscillator in a simulation of the model. Then, Equation 16 shows the update rule for the phase of a single oscillator, with the last four terms corresponding to the four aforementioned qualities.

$$\theta_i \leftarrow \theta_i + dt(\omega_i + Kr\sin(\psi - \theta_i)) + \alpha\mathcal{N}\left(0, \sqrt{dt}\right) + \beta z(\theta_i)u_i(t)$$

Equation 16: Update Rule for Extended Kuramoto Model

With such a framework, a neuron is assumed to spike regularly at a given frequency, ω_i; a spike is then modelled as the completion of a cycle by an oscillator, where the time the oscillator takes to complete each cycle is given by the inverse of its frequency, i.e. its period. Figure 8 visualizes a population of 10 oscillators orbiting clockwise; in this visualization, one can assume that an oscillator spikes when it crosses the 0° mark.

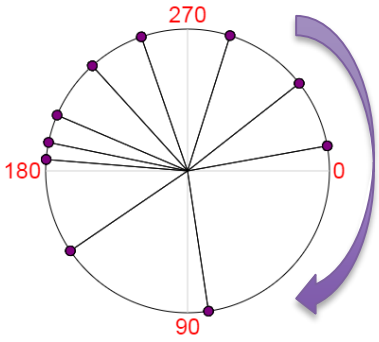

Figure 8: Visualization of Neuronal Oscillators

Another feature of the Kuramoto model is that it models the synchrony of a population of neurons. The strength of synchrony is modulated by the coupling

factor, *K*. In Equation 16, the coupling term, $Kr\sin(\psi - \theta_i)$, includes two order parameters that are calculated at each time step: ψ, which is the population's mean phase, and $r \in [0,1]$, which is the magnitude of the mean vector of the phases plotted on the unit circle and represents the coherence of the population's phases. r close to 1 means the population is highly synchronized (Equation 17).

$$\psi = \frac{1}{N}\sum_{i=1}^{N}\theta_i$$

$$X = \frac{1}{N}\sum_{i=1}^{N}\cos\theta_i\,, Y = \frac{1}{N}\sum_{i=1}^{N}\sin\theta_i$$

$$r = \sqrt{X^2 + Y^2}$$

Equation 17a-c: Order Parameters for Kuramoto Model

Intuitively, the coupling term "speeds up" oscillators that are "behind" the mean phase, ψ, and "slows down" those that are ahead of the mean phase. For instance, if the *i*-th oscillator is "behind" the mean phase, then $\psi - \theta_i > 0$, making the sin term positive and thus the whole coupling term contributes an increase to the phase θ_i in the update rule (Equation 16).

The model also captures the noisiness of neuronal spiking by adding Gaussian noise with a mean of 0 and a standard deviation of $\sqrt{dt}$, which ensures that the effect of the noise does not depend on the size of the time step, and then scaling the Gaussian noise by the noise constant, α.

Finally, the extended model incorporates DBS in the last term of the update rule. The function, $z(\theta_i)$: $[0,2\pi] \rightarrow [0,1]$, represents the phase response function of an individual neuron, as previous work has demonstrated that a neuron's response to stimulation is phase-dependent (Best, 1979; Guttman et al., 1980). Typically, in the literature, the phase response function takes on a sinusoid function, i.e. $z(\theta_i) = \cos\theta_i$ (Tass, 2003). Note that this is similar yet not the same as the change in phase of an aggregate population of neurons or that of a behavioral output like a hand tremor. Being able to derive an appropriate phase response function of an individual neuron from aggregate populations remains an area of active research (Netoff et al., 2012; Wilson and Moehlis, 2015). Next, the stimulation function $u_i(t)$ denotes whether the *i*-th oscillator is stimulated at time *t* (Equation 18). The parameterization of $u_i(t)$ by oscillator allows for DBS to effect only a sub-population of oscillators. Lastly, the DBS strength parameter, β, scales the phase-dependent and oscillator-specific effect of DBS.

$$u_i(t) = \begin{cases} 1, & \text{if oscillator } i \text{ is stimulated at time } t \\ 0, & \text{otherwise} \end{cases}$$

Equation 18: Tass, 2003's Stimulation Function

This extended Kuramoto model can be used to model tremor amplitude by averaging the cosine parts of the phases (Equation 19).

$$a(t) = \frac{1}{N}\sum_{i=1}^{N}\cos[\theta_i(t)]$$

Equation 19: Modeling Tremor Amplitude

In summary, the free model parameters are oscillator frequencies, $\{\omega_i | i = 1, \dots, N\}$, the coupling constant, K, the noise constant, α, and the DBS strength constant, β. Additionally, the number of oscillators, N, and the size of the time step, dt, must be chosen. With $\beta = 0$, the update rule is reduced to the typical formulation of the Kuramoto model; thus, the DBS term was the primary theoretical extension from Tass' work.

Stimulation Function Extension on Tass, 2003

First, for this project, the assumption is made that stimulation instantaneously affects oscillators at the same time; the binary indicator function, $i(t)$, indicates if when stimulation is being given at time t (Equation 20). Further work could be done to explore using different time delays for different oscillators, simulating the time it takes for a pulse to travel to a neuron.

$$i(t) = \begin{cases} 1, & \text{if stimulation is given at time } t \\ 0, & \text{otherwise} \end{cases}$$

Equation 20: Indicator Function for Stimulation

For this project, four different stimulation functions $u_i(t)$ were tested to investigate more biologically plausible models of DBS. Unless otherwise specified, throughout the rest of the dissertation, $u_i(t)$ in the update rule (Equation 16) will be denoted $u_*(i,t)$ where the asterisk indicates which stimulation effect function is being used. A stimulation function $u_*(i,t)$ (Equation 21) captures if stimulation is being given at time t with the indicator function $i(t)$ as well as what kind of effect stimulation has on a population of neurons with a stimulation effect function $s_*(i)$.

$$u_*(i,t) = i(t) \times s_*(i)$$

Equation 21: General form for Stimulation Function

First, a uniform stimulation effect function, $s_u(i)$, that decoupled DBS strength from the number of oscillators, was developed (Equation 22). Using $s_u(i)$, the uniform stimulation function $u_s(i,t)$ is most similar to the one used in Tass, 2003, except that it assumes that stimulation affects all oscillators instantaneously.

$$s_u(i) = \frac{1}{N}$$

Equation 22: Uniform Stimulation Effect Function

Next, a random stimulation effect function, $s_r(i)$, was developed in an attempt to capture the effect that a thalamic neuron's response to DBS is likely proportional to its distance from the DBS electrode. This function first draws *N* samples from the standard uniform distribution and then normalizes them (Equation 23). The weights of DBS stimulation effect are fixed after the simulation is initialized, when the *N* uniform samples are drawn and normalized.

$$x_i \leftarrow \mathcal{U}(0,1)$$
$$s_r(i) = \frac{x_i}{\sum_{j=1}^{N} x_j}$$

Equation 23a-b: Random Stimulation Effect Function

Additionally, a "half" stimulation effect function, $s_h(i)$, is presented in order to naively model the phenomenon that two neuronal populations, one in the motor cortex and one in the thalamus, might contribute to Parkinsonian-like tremor; however, only the thalamus is stimulated; thus, DBS should only effect one population (Equation 24).

$$s_h(i) = \begin{cases} \frac{2}{N}, & \text{if } i \leq \frac{N}{2} \\ 0, & \text{otherwise} \end{cases}$$

Equation 24: Half Stimulation Effect Function

Lastly, a "mixture" stimulation function, $s_x(i)$, attempts to capture both qualities of the random and "half" stimulation functions (Equation 25).

$$y_i \leftarrow \begin{cases} \mathcal{U}(0,1), & \text{if } i \leq \frac{N}{2} \\ 0, & \text{otherwise} \end{cases}$$
$$s_x(i) = \frac{y_i}{\sum_{j=1}^{N} y_j}$$

Equation 25: Mixture Stimulation Effect Function

Note that for all functions, , $\sum_{i=1}^{N} s_*(i) = 1$. This normalization was added to make DBS strength independent from *N* and to make the stimulation effect functions comparable to one another, as the same amount of DBS is distributed to all oscillators.

Optimized Model Parameters

In collaboration with lab member Dr. Gihan Weerasinghe, model parameters parameters were found via a non-linear optimization that minimized the least

square error between qualities of the model-generated data and those of one patient whose hand tremor was recorded in the absence of DBS (the patient was included in the Cagnan et al., 2013 study). The optimization fitted the model based on the following two qualities: 1. the power spectrum of the data, and 2. the probability of obtaining a particular tremor amplitude. When using N = 10 oscillators, these optimized model parameters were found: $\omega_i \leftarrow \mathcal{N}(\mu = 32.3319, \sigma = 2.5804)$, $K = 1.89753$, and $\alpha = 2.66466$. Given in radians per second, the mean angular frequency from which oscillator frequencies were drawn corresponds roughly to a bit more than 5Hz, which is close to the natural 4-6Hz frequency at which Parkinsonian and essential tremors occur. Unless otherwise noted, the above parameters were used in simulations reported in the Results section.

Simulating Phase-Locked DBS

Unless otherwise specified, model simulations explained in the Results section used the aforementioned optimized parameters as well as the following parameters chosen a priori: $\beta = 0.5$, $dt = 1/2048$, $N = 10$. Additionally, unless otherwise noted, model simulations were designed to mimic the experimental set-up, with a simulation block consisting of 1 second of no stimulation followed by 5-seconds of phase-locked 130Hz, 6-pulse stimulation at 12 phases, i.e. $\{0°, 30°, \ldots, 330°\}$. The phase at which DBS was locked to was simply the mean phase of the oscillator population, which was calculated at each time step (Figure 9, 3rd row). At the start of each block, phases were uniformly drawn from the interval $[0,2\pi]$. Similar to the experimental design, 9 blocks were simulated for each of the 12 phases.

Similar preprocessing was conducted on the simulated data: while the simulated data was not resampled to 1000Hz like the experimental data, it was band-pass filtered between 3-6Hz in the same way (Figure 9, 2nd row). The amplitude and instantaneous frequency were also calculated in the same fashion and the same changes in amplitude, frequency, and phase metrics were calculated on the simulated blocks as well as the same statistical analysis. The principal aim of the simulations was to reproduce the same effects observed in the experimental data by primarily investigating what phase response curve yielded the most experimentally-consistent results. Additional analysis was conducted to explore the limits of the model in explaining the experimental data and is described in the Results section.

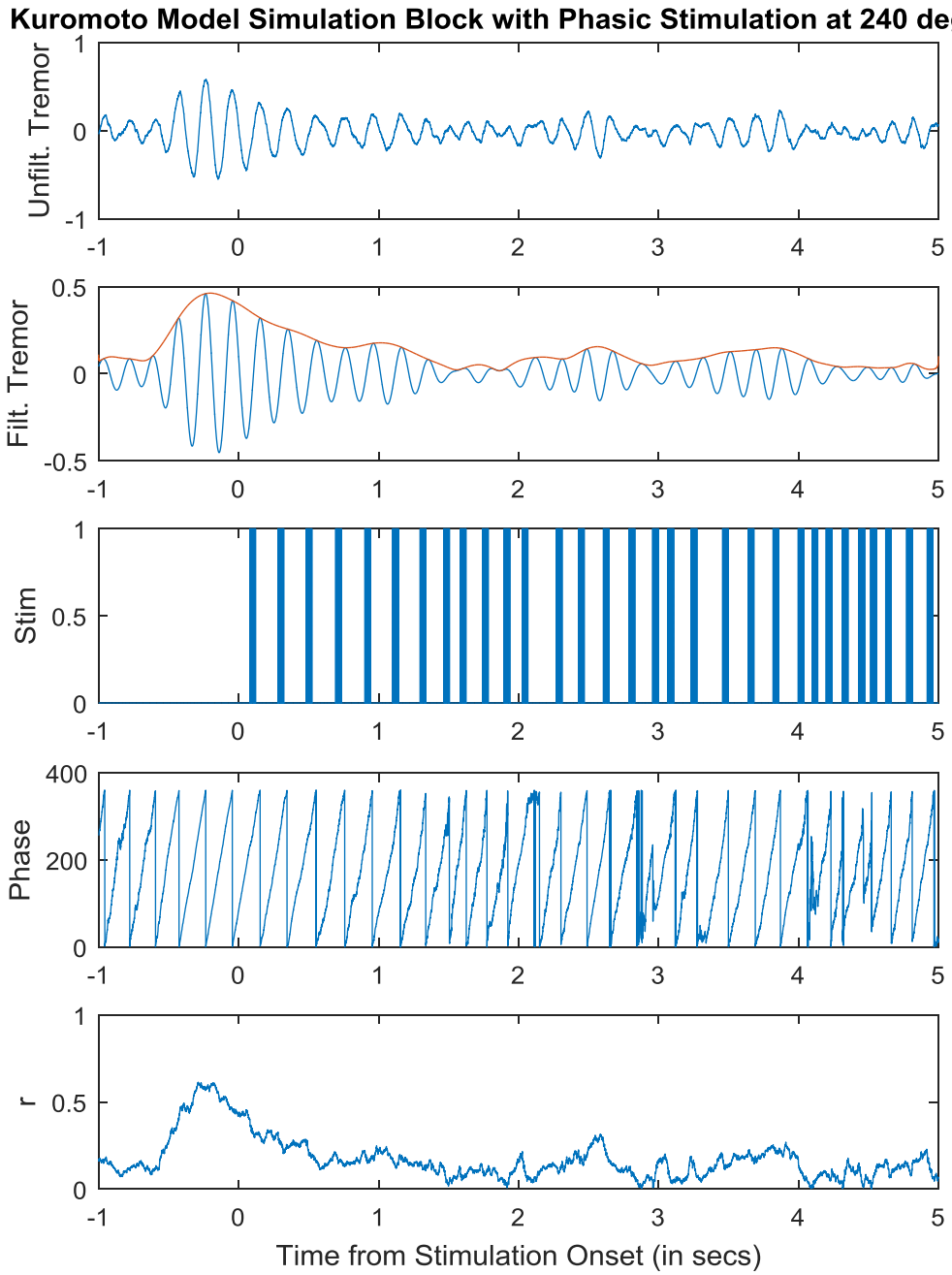

Figure 9: Simulated Block with Phasic Stimulation at 240° using Default Parameters

(1st row) Simulated, unfiltered tremor acceleration signal, calculated using Eqn 19. (2nd row) Filtered tremor signal and amplitude (orange line). The tremor signal from the 1st row was band-passed filtered between 3Hz and 6Hz; the tremor amplitude was derived via the analytical signal. (3rd row). 35ms of 130Hz DBS was administered when the filtered tremor signal passed the 240° phase, as tracked in the 4th row. (4th row) Mean phase of the oscillator population. (5th row) Coherence metric. r connotes how synchronized the population of oscillators is.

Extended Kuramoto Model Online Simulation Tool & Tutorial

As part of a public engagement event with local Oxfordshire high school students, an online simulation of the model used in this project was built (1002072, 2016b). It was also used for research to qualitatively understand the model and observe how certain parameter changes affected the model. Additionally, an intuitive online tutorial of the model was developed (1002072, 2016c). Appendix 4 provides more details about the tool.

Results

Analysis of Experimental Data

An analysis of the change in amplitude, frequency, and phase for all 107 experimental blocks demonstrated a statistically significant phase-dependent suppression of tremor when phase-locked DBS is administered around 210°-240°. The change in amplitude, frequency, and phase were calculated according to the metrics described in the Methods section.

Change in Amplitude, Frequency, and Phase Curves

When the change in tremor amplitude for all blocks are plotted (Figure 10, 1st row), there appears to be a suppressive effect at 120° and 240° and an amplifying effect at 30°, which diametrically opposes 210°. Note that all but two 240° blocks yielded a tremor-suppressive effect, and all but three 210° blocks did the same.

When the change in instantaneous frequency of the filtered tremor amplitude for all blocks are plotted (Figure 10, 2nd row), there appears to be a maximum peak at 240° and a minimum peak at 60°, which diametrically opposes 240°.

When the change in phase for all blocks are plotted (Figure 10, 3rd row), there is a global, maximum peak 240° and global, minimum peak at 60°, which diametrically opposes 240°. There also is a local, maximum peak at 150° and a local, minimum peak at 180°.

Most notably, at 240°, the most tremor-suppressing phase at which to phase-lock DBS to, the tremor-suppressing effect captured in the change in amplitude curve is correlated with a maximal speed-up in frequency and phase.

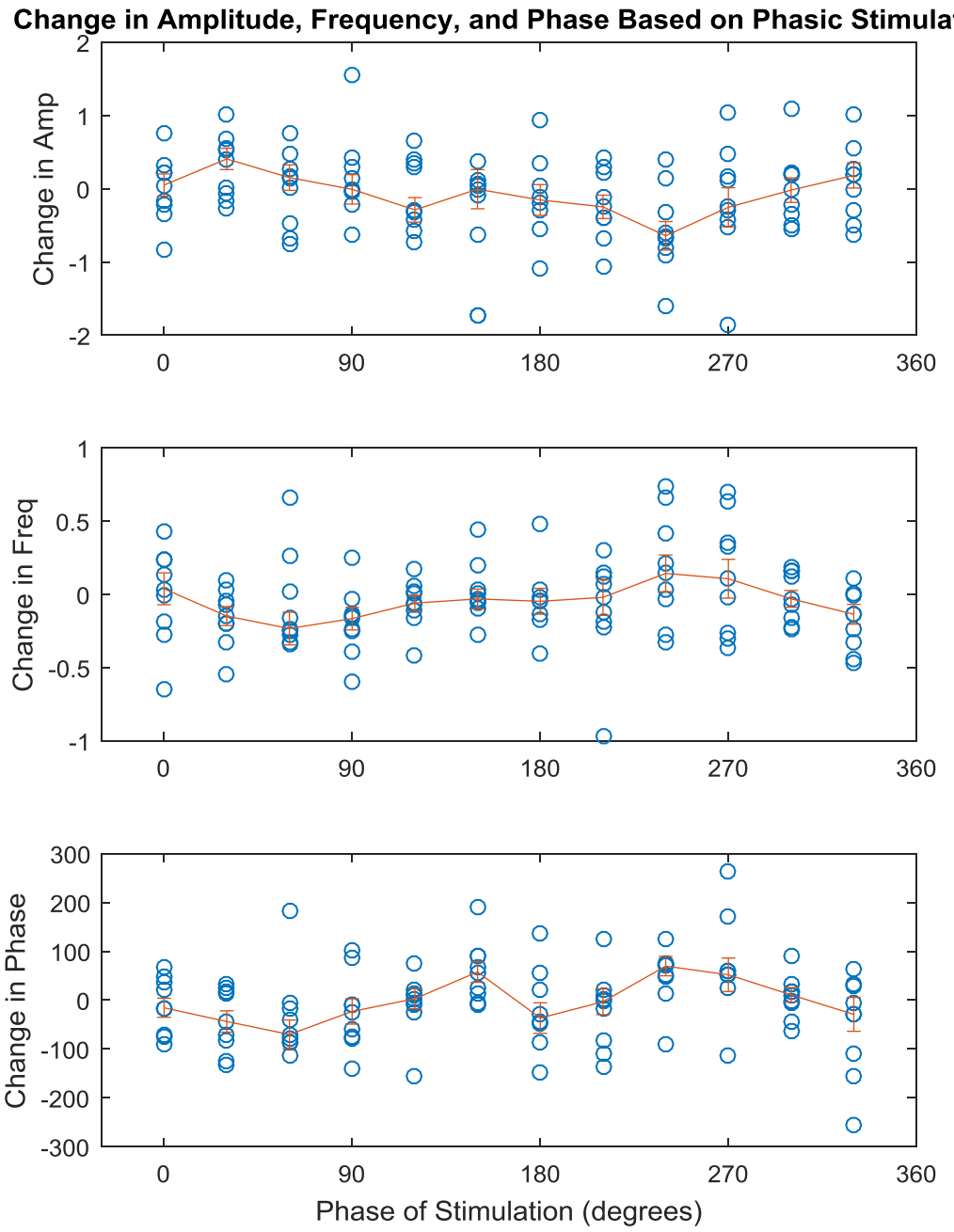

Figure 10: Change in Amplitude, Frequency, and Phase of Experimental Data

The change in amplitude (in m/s^2), Δa (1st row), frequency (in Hz), Δf (2nd row), and phase (in degrees), $\Delta\theta$ (3rd row), were calculated for all 107 experimental blocks and plotted above (blue circles). Linear interpolations of the median Δa, Δf, and $\Delta\theta$ for each phase of stimulation were plotted (orange lines) along with standard error.

Significance Testing

To test whether the palpable suppressive effects in the change in tremor amplitude as well as the seemingly-phase dependent change in frequency and phase metrics are statistically significant, the weighted Moore-Rayleigh and Scaled Rayleigh permutation tests were used. For each test run, 100,000 samples with a sample size of 100 – comparable in size to the 107 experimental blocks – were used to generate the null distribution with which to compare the critical z score of the relevant test to.

	p-value		Phase of resultant vector	
	Moore-Rayleigh	*Scaled Rayleigh*	*Moore-Rayleigh*	*Scaled Rayleigh*
$\Delta \boldsymbol{a}$	0.0056	0.0067	31.7°	30.9°
$-\Delta \boldsymbol{a}$	0.0190	0.0065	216.6°	210.9°
$\Delta \boldsymbol{f}$	0.0470	0.0422	241.3°	240.6°
$\Delta \boldsymbol{\theta}$	0.0104	0.0130	232.6°	222.7°

Table 1: p-values and Result Phases from Moore-Rayleigh and Scaled Rayleigh Significance Testing of Change in Amplitude, Frequency, and Phase of Experimental Data

According to these tests, there was significant non-uniformity ($p < 0.05$) for all metrics (Table 1). Tests were conducted for the negative change in amplitude, $-\Delta a$, to test significant depression, as opposed to significant amplification (Figure 11, top plot). The test for change in amplitude, Δa, still provides some information as to the direction of the non-uniformity. The diametrically opposite phases of those test's phases of the resultant vector, 31.7° and 30.9° for the Moore-Rayleigh and Scaled Rayleigh tests, are 211.7° and 210.9° respectively. The phases of the tests' resultant vectors are all within the range 210°-242°. Note that these phases are not themselves statistically significant metrics but simply show the mean direction of weighted non-uniformity. They are likely skewed to be less than 240° because there is a small tremor suppressing effect for 120° phase-locked DBS.

Figure 11 visualizes the tremor suppressive effect, as well as the correlated amplification of change in frequency and phase, when DBS is phase-locked around 210°-240°, as there are many more data points with greater magnitudes in the third quadrant (corresponding to 180°-270°) than in the other quadrants.

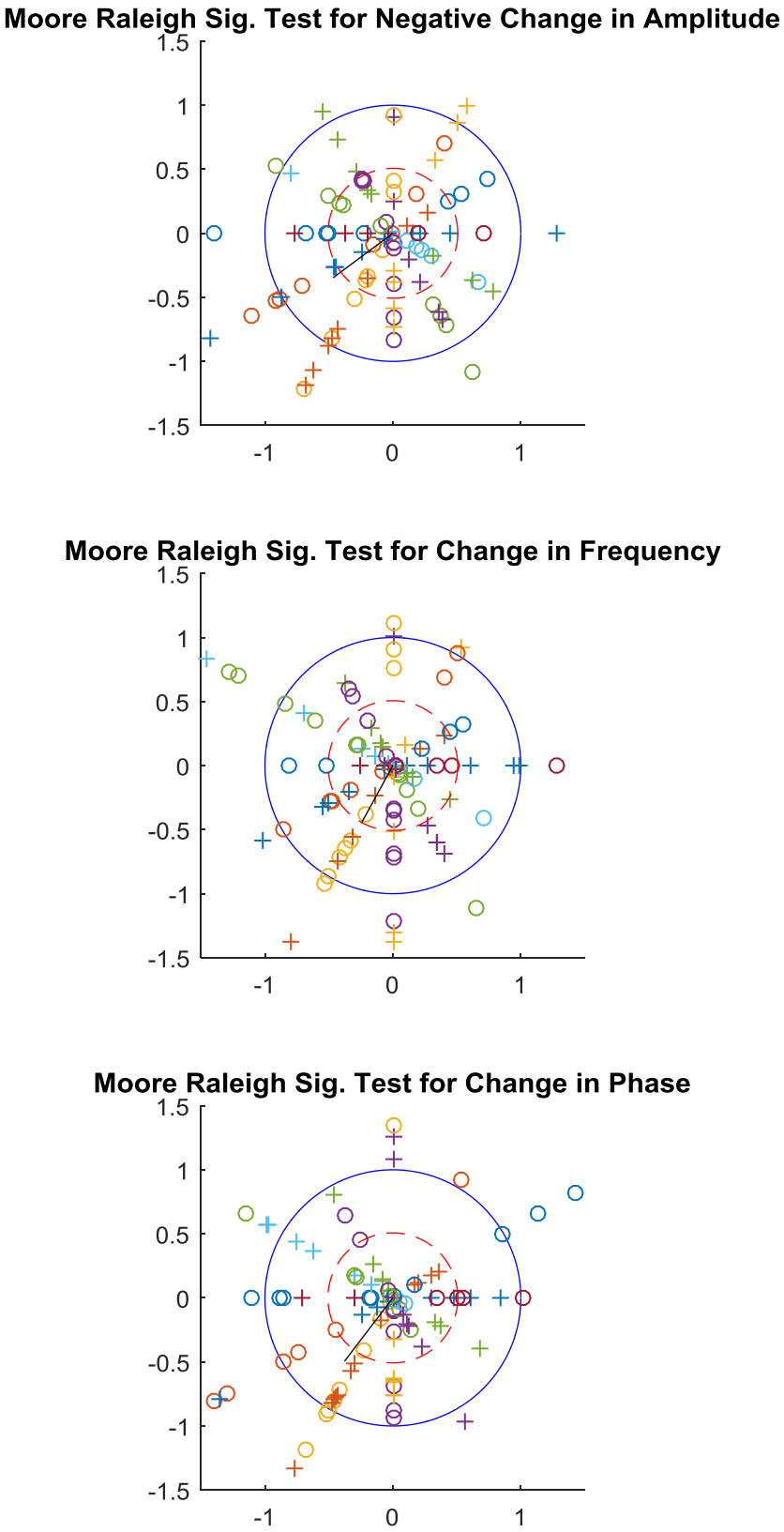

Figure 11: Visualizations of Moore-Rayleigh Test for Negative Change in Amplitude, Change in Frequency, and Change in Phase

The z-score normalized values of the negative change in amplitude (top plot), change in frequency (middle plot), and change in phase (bottom plot) metrics for all 107 experimental blocks are plotted by their phases on the unit circle as polar coordinates, i.e. $(\theta_i, -\Delta a_i)$, $(\theta_i, \Delta f_i)$, and $(\theta_i, \Delta\theta_i)$ respectively. The metrics for the 8-9 blocks associated to a same phase are colored by the same color. "+" markers denote a positive metric value while "o" markers denote a negative metric value; negative values are plotted in the direction of the diametrically-opposite phase. The $p < 0.05$ threshold from the Moore-Rayleigh permutation test is plotted as the dotted red circle, and the Moore-Rayleigh critical z-score of the experimental data is plotted as the magnitude of the black vector, whose phase denotes the phase of the resultant vector. For space efficacy, the visualization is restricted to plot points with magnitudes less than 1.5.

Correlation among Change in Amplitude, Frequency, and Phase

Change in amplitude is negatively related to change in frequency and change in phase; while change in frequency and change in phase are strongly positively correlated. The correlation coefficients and corresponding p-values were computed between the 107 change in amplitude values and those of the change in frequency metric; the same comparison was done for the other pairings of the three metrics (Table 2). The strong, positive correlation between change in frequency and change in phase is to be expected, as the change in phase metric is simply a different method for calculating frequency (by unwrapping the actual phase of the filtered tremor signal).

	R (correlation coefficient)	p-value
$\Delta\boldsymbol{a}$ vs. $\Delta\boldsymbol{f}$	-0.4077	1.3052×10^{-05}
$\Delta\boldsymbol{a}$ vs. $\Delta\boldsymbol{\theta}$	-0.4021	1.7618×10^{-05}
$\Delta\boldsymbol{f}$ vs. $\Delta\boldsymbol{\theta}$	0.6735	1.8956×10^{-15}

Table 2: Correlation between Change in Amplitude, Frequency, and Phase of Individual Experimental Blocks

The correlation coefficients and p-values of correlation were computed on the 107 values of the change in amplitude, frequency, and phase metrics.

From the analysis of experimental data, phase-locked DBS around 240° best suppresses tremor (Figure 10, 1st row). Furthermore, tremor suppression around 240° corresponds to maximal increases in frequency and phase across all phases (Figure 10, 2nd and 3rd rows).

Analysis of Modelled Data

Predicting a Consistent Tremor Suppressive Model

Assume that all thalamic neurons respond to DBS in exactly the same phase-dependent fashion, that is, that the effect of DBS on one neuron at a particular time is identical to that on another neuron. Then, based on Tass, 2003 extension of the Kuramoto model, assuming that DBS affects all oscillators indiscriminately and instantaneously, the most optimal phase at which to stimulate should be the phase

at which the phase response curve (PRC) function of an individual neuron, $z(\theta_i)$, has the steepest, positive slope (Wilson and Moehlis, 2014).

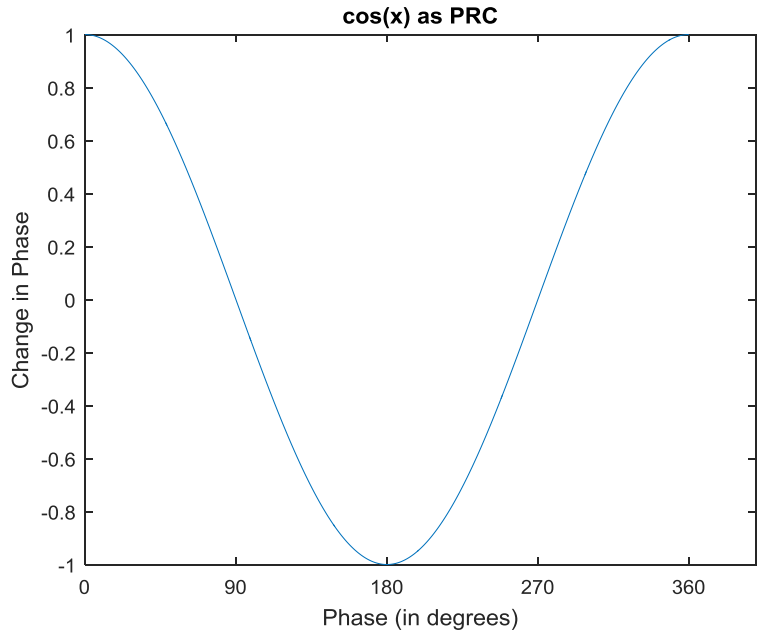

Figure 12: Cosine Curve as Individual Neuron's Phase Response Curve (PRC)

Suppose that the PRC for all oscillators was $z(\theta_i) = \cos(\theta_i)$ (Figure 12). Then, the slope of the PRC is most steeply positive, i.e. $z'(\theta_i)$, the derivative of the PRC, has a maximum point, at phase 270°. If a population of Kuramoto oscillators with the cosine function as its PRC is "stimulated" when the population's mean phase is 270°, the oscillators will become more desynchronized. This is because the oscillators with phases greater than 270° will speed up, because $z(270° + \varepsilon) > 0$, while the oscillators with phases less than 270° will slow, because $z(270 - \varepsilon) < 0$ (Figure 13).

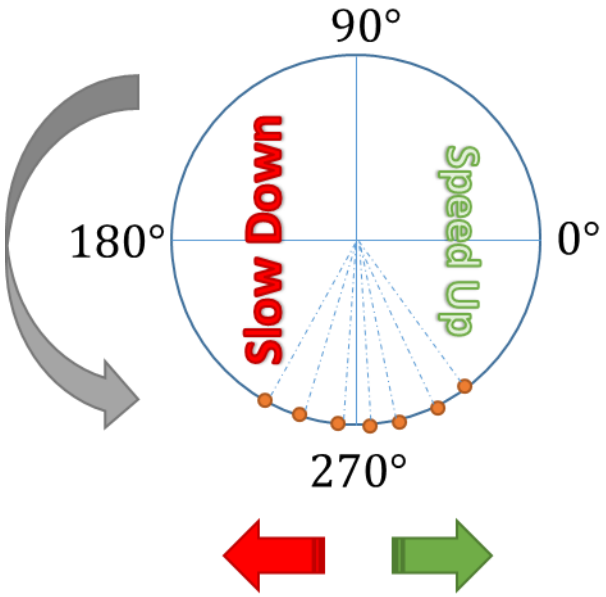

Figure 13: Diagram of the Optimal Stimulation Strategy for the Kuramoto Model

Kuramoto oscillators (orange circles) are oscillating counter-clockwise (indicated by the gray arrow). If the oscillators' PRC function is $z(\theta_i) = \cos(\theta_i)$, then the optimal phase of stimulation is when the mean phase of the oscillators is equal to 270°. This is because the oscillators whose phases are greater than 270° will speed up while those whose phases are less than 270° will slow down, thereby desynchronizing the population.

Based on this interpretation of the extended Kuramoto model, to model maximal tremor suppression at 240° as was observed in the experimental data, a PRC such as $z(\theta_i) = \cos(\theta_i + \frac{\pi}{6})$ should be used, because the curve is most positively sloped and crosses the y-axis at 240° (Figure 14).

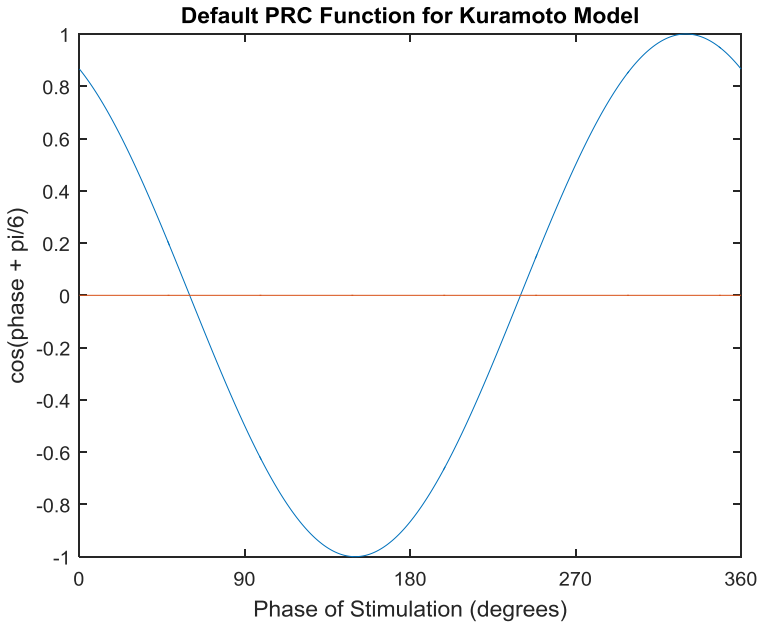

Figure 14: Default PRC function, $z(\theta_i) = \cos(\theta_i + \frac{\pi}{6})$, for Extended Kuramoto Model

Default Parameters for Extended Kuramoto Model

Unless otherwise mentioned, the following default parameters are used to simulate the Kuramoto model (Equation 16).

These parameters were found via an optimization that chose the parameters that best simulated tremor signal of an essential tremor patient in the absence of DBS:

- Initial phases of oscillators = $\theta_i \leftarrow \mathcal{U}([0,2\pi])$
- Angular frequency of oscillators: $\omega_i \leftarrow \mathcal{N}(\mu = 32.3319, \sigma = 2.5804)$,
- Coupling constant: $K = 1.89753$,
- Noise constant: $\alpha = 2.66466$,

These parameters were fixed *a priori*:

- Number of oscillators: $N = 10$,
- Time step: $dt = 1/2048$,
- DBS strength constant: $\beta = 0.5$,
- PRC function: $z(\theta_i) = \cos(\theta_i + \frac{\pi}{6})$,
- Stimulation function: $u_u(i,t) = i(t) \times \frac{1}{N}$

To simulate the experimental trial, 6-second blocks of the Kuramoto model were simulated, in which 1 second of no stimulation was followed by 5 seconds of 130Hz, 6-pulse stimulation locked to a specific phase. 108 blocks were simulated, 9 blocks for each of the 12 phases, i.e. $\{0°, 30°, \ldots, 330°\}$. 9, 6-second reference blocks, in which no DBS was administered, were also simulated and used as a baseline to compare with which to compare the phase-locked-DBS simulated blocks.

See the Methods section for more details on how parameters were chosen and the simulations were executed.

Results using Default Parameters

When simulating the experimental set-up using the extended Kuramoto with the aforementioned default parameters, statistically significant tremor suppression was observed (Table 3). However, the model failed to provide an explanation for the simulated suppression that was consistent with the experimental data for tremor suppression.

Change in Amplitude, Frequency, and Phase

The same change in amplitude, frequency, and phase metrics were computed on the simulated as was done on the experimental data.

From the change in amplitude curve, tremor suppression appeared strongest in simulated blocks in which DBS was phase-locked to 180°-270° (Figure 15, 1st row). This broad suppression effect for phases 180°-270° differs from that observed in the

experimental data (Figure 10, 1st row), which had a small suppressive effect at phase 150° and another at 240°.

While the relationship between the change in amplitude (Figure 15, 1st row) and change in frequency curves (Figure 15, 2nd row) is not apparent without further analysis, tremor suppression for phase-locked stimulation at 180°-270° (Figure 15, 1st row) appears correlated to the positive slope and zero-crossing in the change in phase curve at 180°-270° (Figure 15, 3rd row). Quantitatively, Table 6 confirms this relationship and shows that the change in amplitude, Δa, is negatively correlated to the derivative approximation of the change in frequency, $\frac{d}{d\theta}(\Delta f)$, $(R = -0.64, p = 0.02)$ as well as to the derivative approximation of the change in phase, $\frac{d}{d\theta}(\Delta\theta)$ $(R = -0.76, p = 0.004)$.

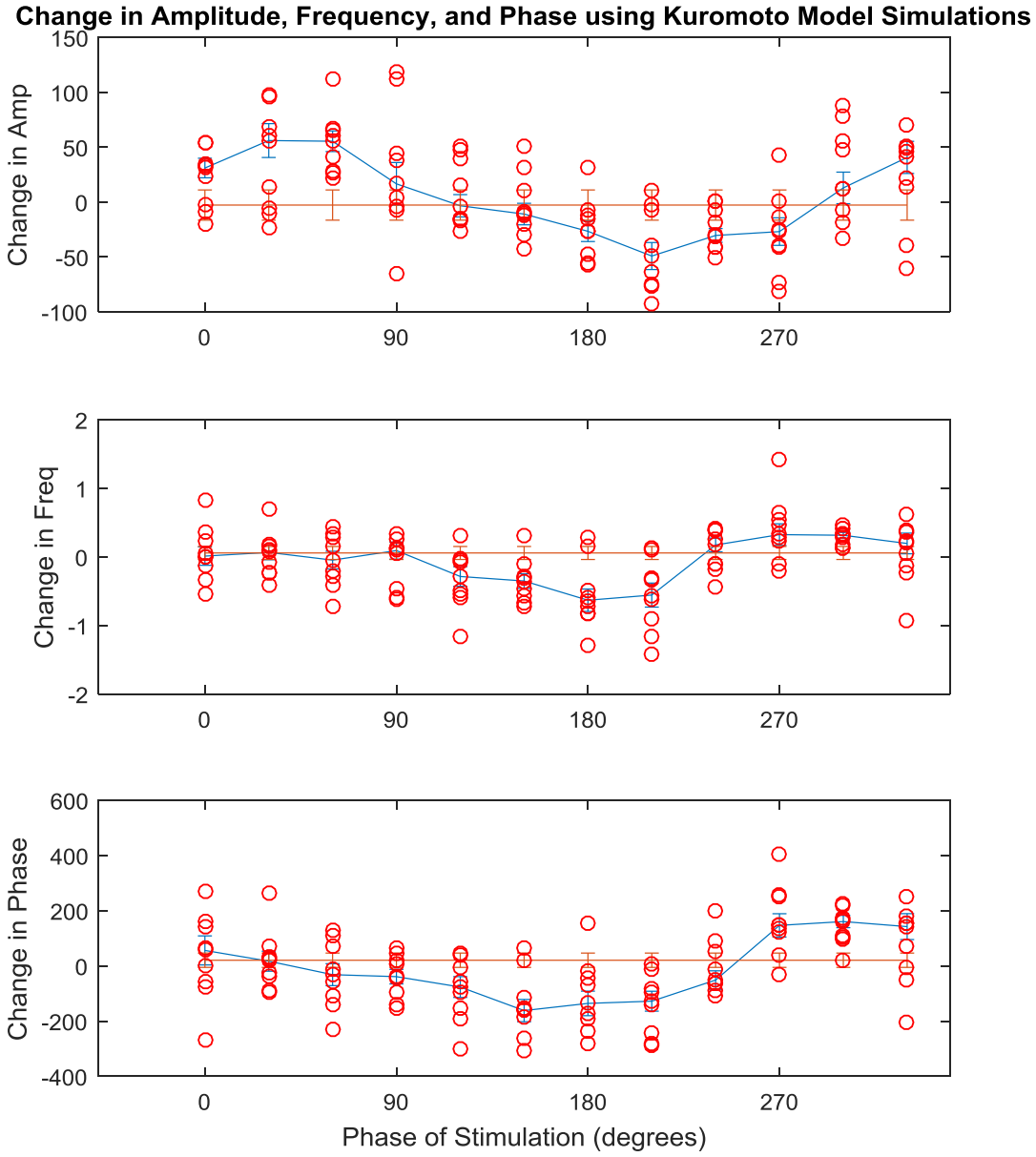

Figure 15: Change in Amplitude, Frequency, and Phase of Simulated Data using Default Parameters

The change in amplitude (m/s^2), Δa (1st row), frequency (Hz), Δf (2nd row), and phase (degrees), $\Delta\theta$ (3rd row), were calculated for all 108 simulated blocks and plotted above (red circles). Linear interpolations of the median $\Delta a, \Delta f$, and $\Delta\theta$ for each phase of stimulation were plotted (blue lines) along with the standard error. The median change in amplitude, frequency, and phase for the 9 reference blocks of no stimulation were also plotted (orange lines).

Significant Testing

The same weighted Rayleigh tests were used to determine whether there was significant non-uniformity in the change in amplitude, frequency, and phase curves for the simulated data. These tests report quite high confidence in a non-uniform

effect for all curves (Table 3). While not a rigorous statistic, the phases of the resultant vectors from these tests for change in amplitude (Table 3) compared to those of the experimental data (Table 1) suggest that the model may roughly have a similar tremor suppression effect around 210°-240°. However, the phases of the resultant vectors for change in frequency and phase tests on the simulated data, i.e. 320°-330°, are nearly perpendicular to those for the corresponding experimental tests, i.e. 220-240°. This suggests that the model may not explain the phase-dependent tremor suppression of this particular patient. Visualizations of the Moore-Rayleigh test for the negative change in amplitude, change in frequency, and change in phase are provided in Figure 16.

	p-value		Phase of resultant vector	
	Moore-Rayleigh	*Scaled Rayleigh*	*Moore-Rayleigh*	*Scaled Rayleigh*
$\Delta \boldsymbol{a}$	$< 10^{-6}$	$< 10^{-6}$	34.8°	36.4°
$-\Delta \boldsymbol{a}$	$< 10^{-6}$	$< 10^{-6}$	214.8°	216.4°
$\Delta \boldsymbol{f}$	10^{-6}	10^{-6}	323.8°	328.5°
$\Delta \boldsymbol{\theta}$	$< 10^{-6}$	$< 10^{-6}$	323.0°	321.7°

Table 3: p-values and Result Phases from Moore-Rayleigh and Scaled Rayleigh Significance Testing of Change in Amplitude, Frequency, and Phase of Simulated Data using Default Parameters

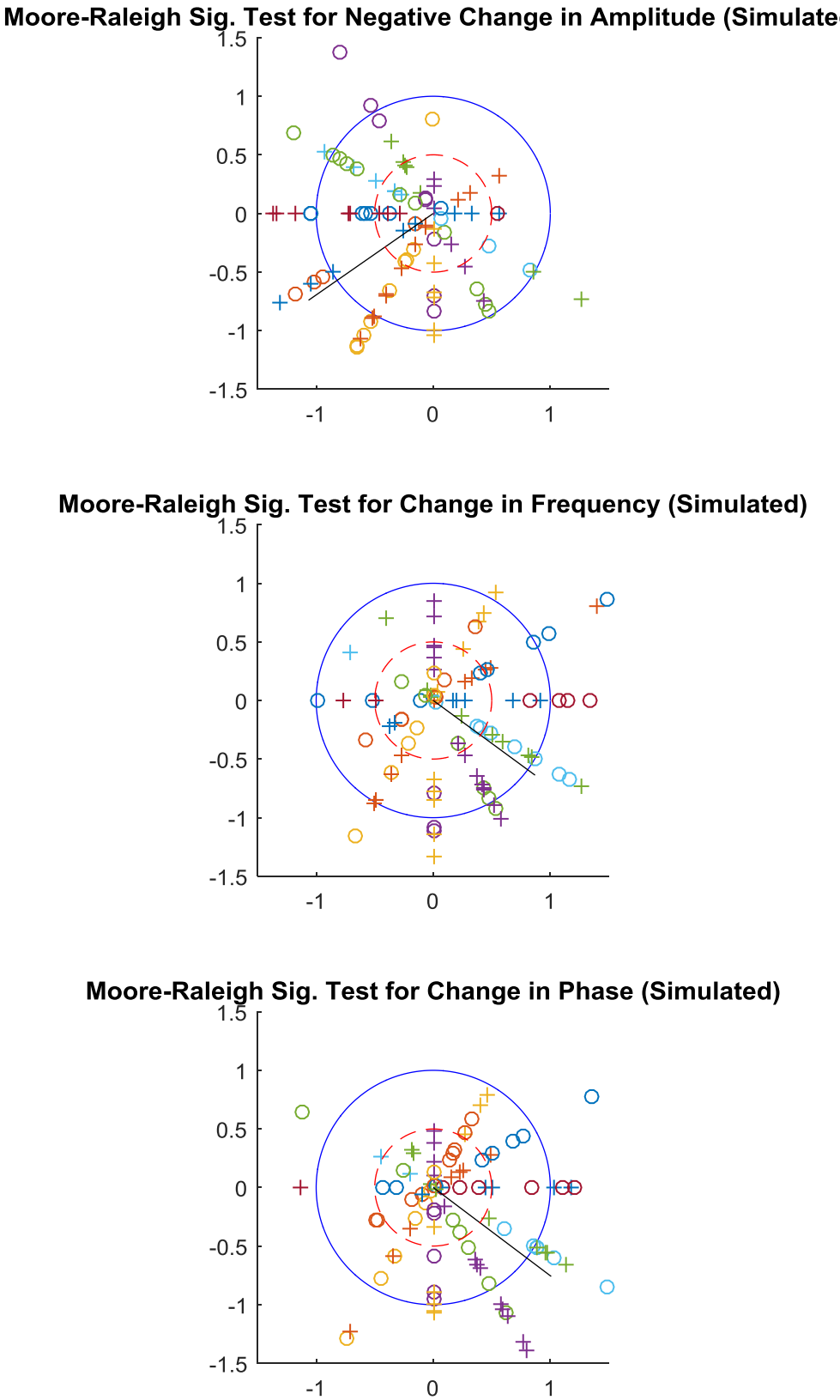

Figure 16: Visualizations of Moore-Rayleigh Test for Negative Change in Amplitude, Change in Frequency, and Change in Phase of Simulated Data using Default Parameters

The z-score normalized values of the negative change in amplitude (top plot), change in frequency (middle plot), and change in phase (bottom plot) metrics for all 108 simulated blocks are plotted by their phases on the unit circle as polar coordinates, i.e. $(\theta_i, -\Delta a_i)$, $(\theta_i, \Delta f_i)$, and $(\theta_i, \Delta\theta_i)$ respectively. The metrics for the 8-9 blocks associated to a same phase are colored by the same color. "+" markers denote a positive metric value while "o" markers denote a negative metric value; negative values are plotted in the direction of the diametrically-opposite phase. The $p < 0.05$ threshold from the Moore-Rayleigh permutation test is plotted as the dotted red circle, and the Moore-Rayleigh critical z-score of the experimental data is plotted as the magnitude of the black vector, whose phase denotes the phase of the resultant vector. For space efficacy, the visualization is restricted to plot points with magnitudes less than 1.5.

Comparison to Experimental Data

To quantify the difference between the simulated and experimental data, the Pearson's correlation coefficients were computed between the corresponding change in amplitude, frequency, and phase curves of the simulated and experimental data (Table 4). There is a significant linear correlation between the change in amplitude effects in the simulated and experimental data, but no such relationship between the change in frequency or phase.

	R (correlation coefficient)	p-value
$\Delta \boldsymbol{a}_{exp}$ **vs.** $\Delta \boldsymbol{a}_{sim}$	0.6437	0.0239
$\Delta \boldsymbol{f}_{exp}$ **vs.** $\Delta \boldsymbol{f}_{sim}$	0.0226	0.9445
$\Delta \boldsymbol{\theta}_{exp}$ **vs.** $\Delta \boldsymbol{\theta}_{sim}$	-0.0093	0.9770

Table 4: Correlations between Median Change in Amplitude, Frequency, and Phase of Experimental Data and those of Simulated Data using Default Parameters

The correlation coefficients and p-values of correlation were computed between the 12 median values of the change in amplitude, frequency, and phase metrics of the experimental data and the 12 median values of the same metrics of the simulated data using default parameters.

Within both the set of experimental blocks and the set of simulated blocks, the correlation coefficients among the different metrics were also computed (Table 5). While there were significant, inverse correlations between change in amplitude and change in frequency (Δa vs. Δf) as well as change in amplitude and change in phase (Δa vs. $\Delta\theta$) among experimental blocks, there were only weak, positive correlations among the same pairs of metrics among simulated blocks.

	R (correlation coefficient)		p-value	
	Experimental	*Simulated*	*Experimental*	*Simulated*
$\Delta \boldsymbol{a}$ vs. $\Delta \boldsymbol{f}$	-0.4077	0.1567	1.31×10^{-05}	0.1053
$\Delta \boldsymbol{a}$ vs. $\Delta \boldsymbol{\theta}$	-0.4021	0.0265	1.76×10^{-05}	0.7857
$\Delta \boldsymbol{f}$ vs. $\Delta \boldsymbol{\theta}$	0.6735	0.6955	1.90×10^{-15}	6.69×10^{-17}

Table 5: Correlation between Change in Amplitude, Frequency, and Phase of Individual Experimental Blocks and Individual Simulated Blocks using Default Parameters

The correlation coefficients and p-values of correlation were computed on the 107 values of the change in amplitude, frequency, and phase metrics of the experimental data (Table 2) and on the 108 corresponding values of the modelled data using default parameters.

Lastly, for both experimental and simulated data, the 12 median values of each curve, corresponding to the 12 phases DBS was locked to, were correlated with each other (Table 6). Additionally, the median values of the change in amplitude curve was correlated with approximations of the derivatives of the change in frequency and in phase. The derivative approximation for a median value at phase θ was computed by taking the difference between the median value at phase $\theta + 30°$ and that at phase $\theta - 30°$. In the experimental data, change in amplitude is strongly, negatively correlated with change in frequency and phase. In contrast, in the simulation data, change in amplitude is strongly, negatively correlated with the derivative approximations of change in frequency and phase. This is expected by Wilson and Moehlis, 2014, which explains that the optimal phasic DBS strategy should be to stimulate at the phase at which the PRC has a positive zero-crossing, that is, where its derivative is most positive. While later simulations demonstrate the population's change in phase curve is a non-linear transformation of the individual PRC function, the change in frequency and phase curves are simply population metrics of the same concept that the PRC function is an individual oscillator's metric for.

	R (correlation coefficient)		p-value	
	Experimental	*Simulated*	*Experimental*	*Simulated*
Δa vs. Δf	-0.7427	-0.0842	0.0057	0.7947
Δa vs. $\frac{d}{d\theta}(\Delta f)$	-0.4774	-0.6447	0.1166	0.0236
Δa vs. $\Delta \theta$	-0.6869	0.0364	0.0136	0.9106
Δa vs. $\frac{d}{d\theta}(\Delta \theta)$	-0.4367	-0.7602	0.1558	0.0041
Δf vs. $\Delta \theta$	0.8246	0.7752	0.000967	0.0031

Table 6: Correlations among Median Change in Amplitude, Frequency, and Phase as well as Select Derivative Approximations of Experimental and Simulated Blocks using Default Parameters

For both experimental and simulated data, the correlation coefficients and p-values of correlation were computed on the 12 median values of the following pairings: 1. change in amplitude and change in frequency, 2. change in amplitude and the derivative approximation of change in frequency, 3. change in amplitude and change in phase, 4. change in amplitude and the derivative approximation of change in phase, and 5. change in frequency and change in phase.

These quantifiable differences between the experimental and simulated data suggest that the model does not explain phase-dependent suppression for the patient from which the experimental data was recorded. While it captures phase-dependent suppression, the extended Kuramoto model proposes the optimal phase at which to stimulate is the one at which there is a positive, zero-crossing in its change in frequency or phase. In contrast, in the essential tremor patient with whom the phase-locked DBS trial was conducted, the optimal strategy appears to be stimulating at the phase at which change in frequency or phase is most positive.

Results using Different Stimulation Functions

From the experimental data, tremor suppression seems correlated to the greatest, positive shift in frequency or phase. It was hypothesized that the greatest phase shift effect yielded the most tremor suppression because DBS desynchronized two sub-populations, speeding up only a portion of neurons. Under this hypothesis, tremor would be most suppressed when a sub-population was most speed up by DBS.

To test this hypothesis and extend the Kuramoto model to better capture this relationship between tremor suppression and change in phase, a few more biologically-plausible stimulation functions were proposed. The "half" stimulation function limits the effect of DBS to half of the oscillator population; this captures the fact that both the thalamus and cortex coordinate motor movements yet DBS only affects a population of thalamic neurons. The "random" stimulation function randomly weighted the effect of DBS on individual oscillators, simulating the varying distances neurons are from the DBS probe. The "mixture" stimulation functions combines both features from the "half" and "random" functions. In the "random" setting, desynchronization was hypothesized to occur between weakly and strongly DBS-affected oscillators, while in the "half" setting, desynchronization was thought to occur between the half sub-population representing DBS-affected thalamic neurons and the other half, representing unaffected, cortical neurons. See the Stimulation Function Extension on Tass, 2003 section for more details about the different stimulation functions.

Simulations modelling the experimental set-up were conducted using each of the above stimulation functions. The Moore-Rayleigh test demonstrated significant non-uniform effects ($p < 10^{-6}$) for the change in amplitude, frequency, and phase curves of all simulations. One confirmation that the simulations were better describing the experimental data would be if the phases of the resultant vectors of the different metrics were roughly around 240°. However, while the phases of the Moore-Rayleigh resultant vectors for the negative change in amplitude curves were in the range of 213°-227.5°, the phases of the resultant vectors for the change in frequency and phase curves were in the range of 315°-330°, a 70°-90° shift from 240°.

Like the simulation using default parameters and the uniform stimulation function, there was significant correlation between the experimental and simulated change in amplitude curves yet none between the change in frequency and phase curves (Table 7).

	R				p-value			
Exp vs. Sim	*Uni*	*Half*	*Rand*	*Mix*	*Uni*	*Half*	*Rand*	*Mix*
$\Delta \boldsymbol{a}_e$ vs. $\Delta \boldsymbol{a}_s$	0.644	0.770	0.811	0.706	0.024	0.003	0.001	0.010
$\Delta \boldsymbol{f}_e$ vs. $\Delta \boldsymbol{f}_s$	0.023	-0.073	-0.080	0.071	0.944	0.821	0.804	0.825
$\Delta \boldsymbol{\theta}_e$ vs. $\Delta \boldsymbol{\theta}_s$	-0.010	0.180	0.119	0.022	0.977	0.576	0.713	0.945

Table 7: Correlations between Median Change in Amplitude, Frequency, and Phase of Experimental Data and those of Simulated Data using Different Stimulation Functions

The correlation coefficients and p-values of correlation were computed between the 12 median values of the change in amplitude, frequency, and phase metrics of the experimental data and the 12 median values of the same metrics of the simulated data using the uniform (Uni), half (Half), random (Rand), and mixture (Mix) stimulation functions.

Similarly, unlike the experimental data, whose change in amplitude and change in frequency and phase curves were strongly, negatively correlated, the only strong correlations within the simulated data for each stimulation function was between change in amplitude and the derivative approximation of change in frequency and phase (Table 8).

	R				p-value			
	Uni	*Half*	*Rand*	*Mix*	*Uni*	*Half*	*Rand*	*Mix*
$\Delta \boldsymbol{a}$ **vs.** $\Delta \boldsymbol{f}$	-0.084	0.477	0.197	0.341	0.795	0.117	0.539	0.279
$\Delta \boldsymbol{a}$ **vs.** $\frac{\boldsymbol{d}}{\boldsymbol{d\theta}}(\Delta \boldsymbol{f})$	-0.645	-0.767	-0.682	-0.596	0.024	0.004	0.015	0.041
$\Delta \boldsymbol{a}$ **vs.** $\Delta \boldsymbol{\theta}$	0.036	0.293	0.047	0.022	0.911	0.355	0.884	0.946
$\Delta \boldsymbol{a}$ **vs.** $\frac{\boldsymbol{d}}{\boldsymbol{d\theta}}(\Delta \boldsymbol{\theta})$	-0.760	-0.670	-0.878	-0.700	0.004	0.017	$< 10^{-3}$	0.011
$\Delta \boldsymbol{f}$ **vs.** $\Delta \boldsymbol{\theta}$	0.775	0.915	0.883	0.794	0.003	$< 10^{-5}$	$< 10^{-5}$	0.002

Table 8: Correlations among Median Change in Amplitude, Frequency, and Phase as well as Select Derivative Approximations of Experimental and Simulated Blocks using Default Parameters

For simulated data using the four stimulation functions, the correlation coefficients and p-values of correlation were computed on the 12 median values of the following pairings: 1. change in amplitude and change in frequency, 2. change in amplitude and the derivative approximation of change in frequency, 3. change in amplitude and change in phase, 4. change in amplitude and the derivative approximation of change in phase, and 5. change in frequency and change in phase.

From these limited simulations, these stimulation functions may not be able to capture the phase-dependent correlation between tremor suppression and positive phase shift of the experimental patient.

Change in Amplitude Curves

When using the "half" stimulation function, there appears to be a broad tremor-suppressing effect at 180°-270° (Figure 17, 1st row). In contrast, when using the "random" stimulation function, there appears to be a sharper, narrower, tremor-suppressing effect at 240°-270° (Figure 17, 2nd row). This is also more similar to the clear, narrow effect observed in the experimental data at 240° (Figure 10, 1st row); the change in amplitude curve for the "random" simulation is also the most correlated with that of the experimental data (Table 7). Lastly, there is a weak, broad tremor-suppressing effect in the "mixture" simulation (Figure 17, 3rd row). More repeated simulations would need to be conducted to rigorously analyze which stimulation function produces a change in amplitude curve most similar to that of the experimental data.

Interestingly, the three curves below (Figure 17) show a small, local minimum around 60°-90° similar to that in the experimental data at 120° (Figure 10, 1st row);

however, unlike the experimental data, these dips in the simulated data are still weak tremor-amplifying effects, as they are above the reference change in amplitude baseline.

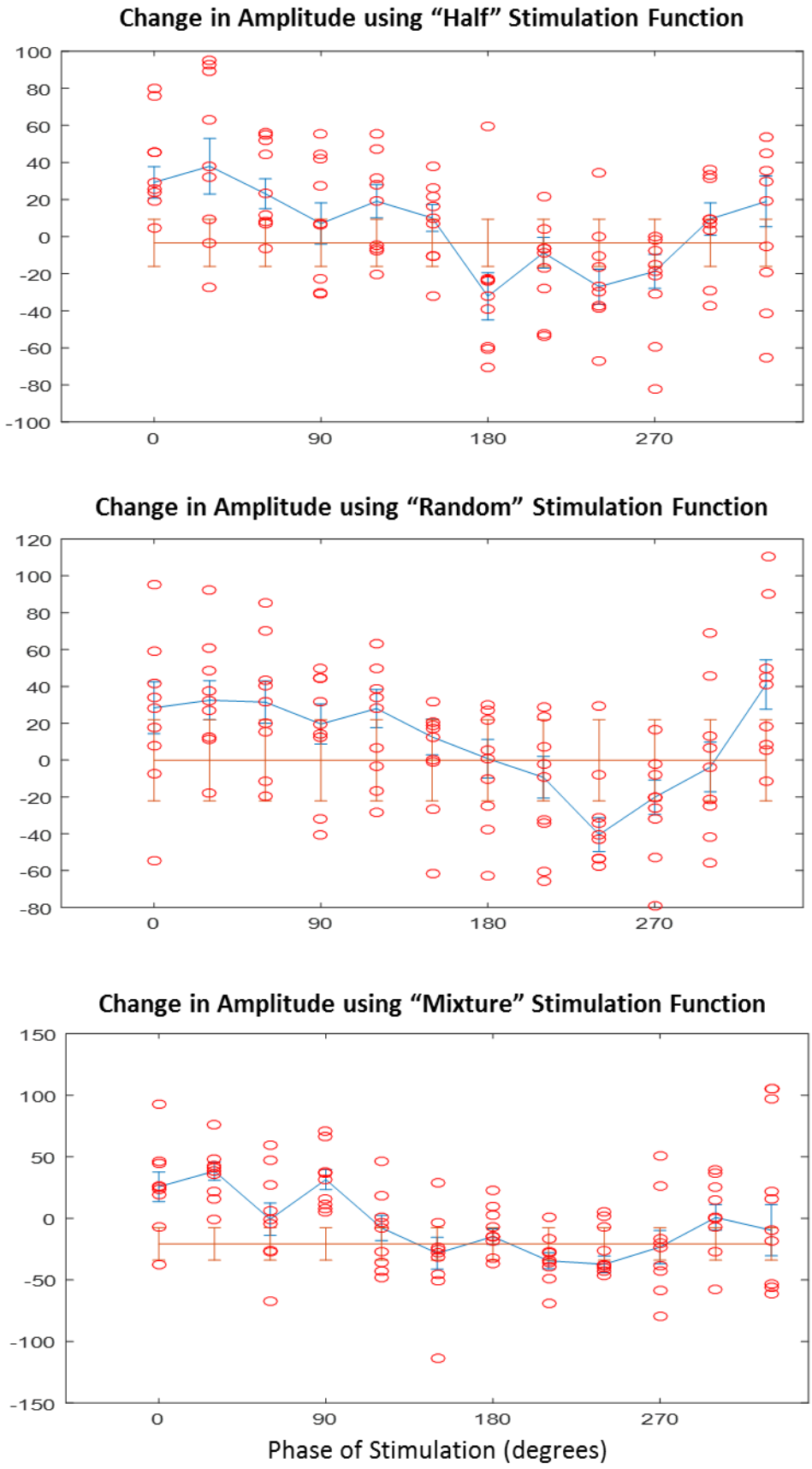
Change in Amplitude using “Half” Stimulation Function
100
80
60
40
20
0
-20
-40
-60
-80
-100
0
90
180
270
Change in Amplitude using “Random” Stimulation Function
120
100
80
60
40
20
0
-20
-40
-60
-80
0
90
180
270
Change in Amplitude using “Mixture” Stimulation Function
150
100
50
0
-50
-100
-150
0
90
180
270
Phase of Stimulation (degrees)

Figure 17: Change in Amplitude Curves for Simulated Data when using "Half", "Random", and "Mixture" Stimulation functions

The change in amplitude, Δa, was calculated for all 108 simulated blocks generated in each simulation using the "Half" (1st row), "Random" (2nd row), and "Mixture" (3rd row) stimulation function and plotted above (red circles). When using each of these stimulation functions, linear interpolations of the median Δa for each phase of stimulation are plotted (blue lines) along with the standard error. The median change in amplitude values for the 9 reference blocks of no stimulation are also plotted (orange lines).

Non-Linear Transformation from Individual PRC to Change in Mean Phase of Oscillator Population

There was a palpable difference between the individual PRC function (Figure 14) used by default, $z(\theta_i) = \cos(\theta_i + \frac{\pi}{6})$, which represents the phase-dependent shift in phase of a single oscillator in response to DBS, and the change in phase curve (Figure 15, 3rd row), which captures the mean phase shift of the oscillator population.

The weakly coupled interactions among oscillators was hypothesized as the reason for this non-linear relationship between the individual neuron's PRC and the population's change in phase curve. To test this hypothesis, simulations were conducted that varied the number of oscillators from 2 to 20 and otherwise used the default model parameters. For each simulation, the mean squared error (MSE) was computed between the individual PRC and the population's median change in phase curve (Figure 18). There is a strong, positive correlation between the number of oscillators used and the oscillator population's divergence from the individual PRC.

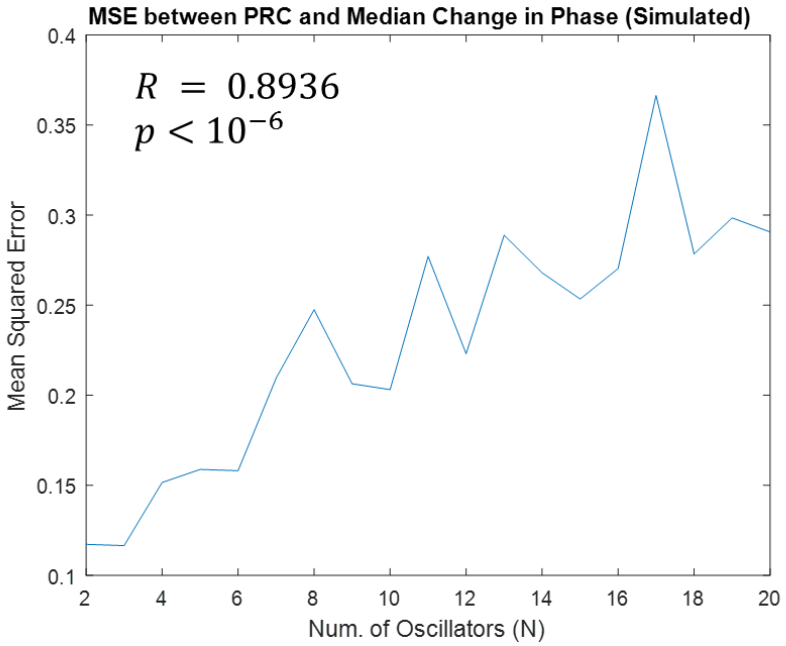

Figure 18: Mean Squared Error between Default PRC Function and Median Change in Phase in Simulated Data as Number of Oscillators Increases

Using the default model parameters and only varying the number of oscillators used, the experimental set-up was simulated once for each $N \in \{2, \dots, 20\}$. The mean squared error (MSE) was calculated between the default PRC function, $z(\theta_i) = \cos(\theta_i + \frac{\pi}{6})$, which represents an individual neuron's phase-dependent response to DBS, and the change in phase curve, like that in Figure 15, 3rd row, from that simulation. The correlation coefficient and corresponding p-value were computed between the number of oscillators, N, and the plotted, corresponding MSE.

Median change in phase curves for simulations using N = 2, 5, and 8 oscillators are included in Appendix 2: Simulated Change in Phase Curves with Different Numbers of Oscillators, where the divergence can be visually observed.

It is reasonable that weak coupling among oscillators would introduce a non-linear transformation between the individual PRC and the population change in phase (Wilson and Moehlis, 2015). This effect adds another layer of complexity to using the extended Kuramoto model, as at best, only a large population of neurons can be recorded in the thalamus or cortex. Note that the experimental data is recording tremor amplitude and phase shifts there, not in the thalamus or cortex; thus, there likely is another transformation from the thalamic and/or cortical population phase shift and that observed in tremor.

Results using Experimental Change in Frequency and Change in Phase Curves as PRC Function

Despite the non-linear transformation discovered above, it was hypothesized that the model may be able to model the change in frequency and phase curves of the experimental data if they were used as the PRC function.

However, the simulations described below show that while using these curves as PRC functions produced somewhat qualitatively similar change in frequency and phase curves to those of the experimental data, they were unable to reproduce change in amplitude curves that were similar to that of the experimental data. This last set of simulations demonstrates the limitation of the Kuramoto model to capture the optimal phasic strategy that worked in the essential tremor patient; the Kuramoto simulations can only match the change in amplitude curve or the change in frequency or phase curves of the experimental data, but not all the curves.

Directly Using Scaled, Experimental Change in Frequency Curve

Using all other default parameters, a linear interpolation of the experimental change in frequency curve (Figure 10, 2nd row) was scaled to range from $[-1, +1]$ and used in a model simulation as the PRC function, $z(\theta_i)$ (Figure 19).

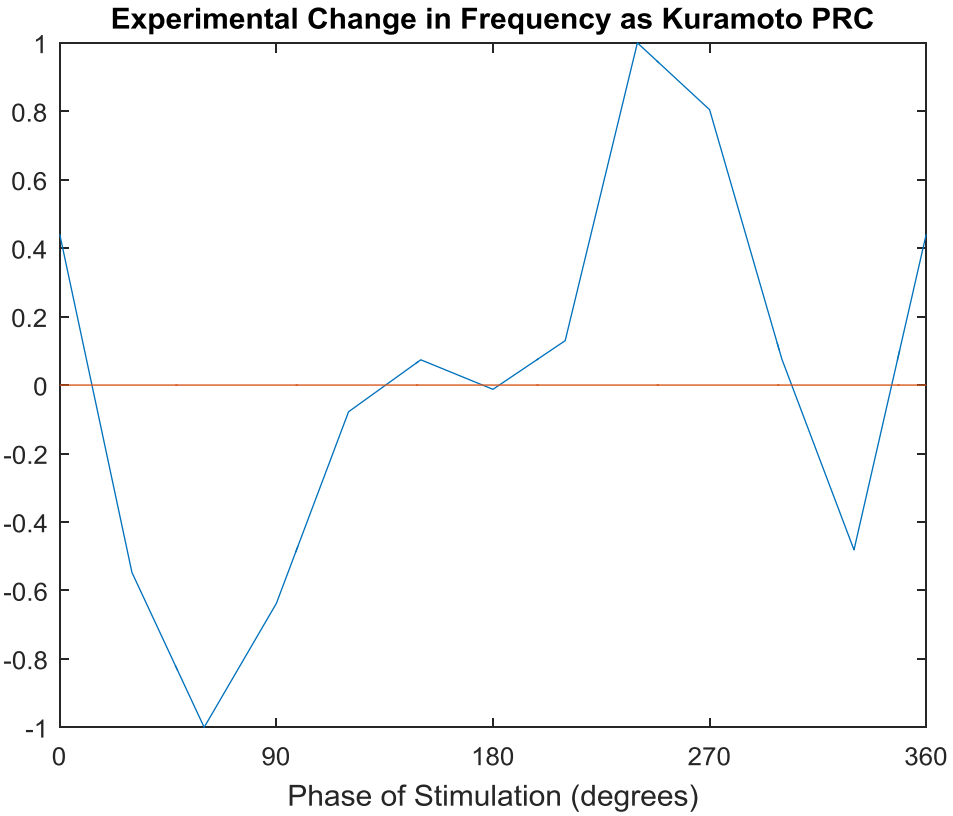

Figure 19: Scaled, Experimental Change in Frequency Curve as PRC Function $z(\theta_i)$ for Extended Kuramoto Model

The linear interpolation of the change in frequency curve from the experimental data (Figure 10, 2nd row) was scaled to range from $[-1, +1]$ and used as the PRC function $z(\theta_i)$ for a simulation of the extended Kuramoto model.

Qualitatively, there appeared to be a broad tremor-suppressing effect at 120°-210° (Figure 20, 1st row), which is roughly a 60° phase shift from the tremor-suppressing effect observed in the experimental data at 240° (Figure 10, 1st row). However, similar to the experimental data, there is a broad peak in the change in frequency and phase curves that includes 210°-270° (Figure 20, 2nd and 3rd rows).

The Moore-Rayleigh test was used on the change in amplitude, frequency, and phase curves and showed significant non-uniformity in all curves ($p < 10^{-3}$). The phases Moore-Rayleigh resultant vectors for the negative change in amplitude, change in frequency, and change in phase curves was 156.1°, 258.1°, and 255.5° respectively. This further corroborates the qualitative observations that, while the change in frequency and phase curves, when using the scaled, change in frequency curve as the PRC function, are more similar to that of the experimental data, the tremor-suppressing effect is now no longer consistent between experimental and simulated data.

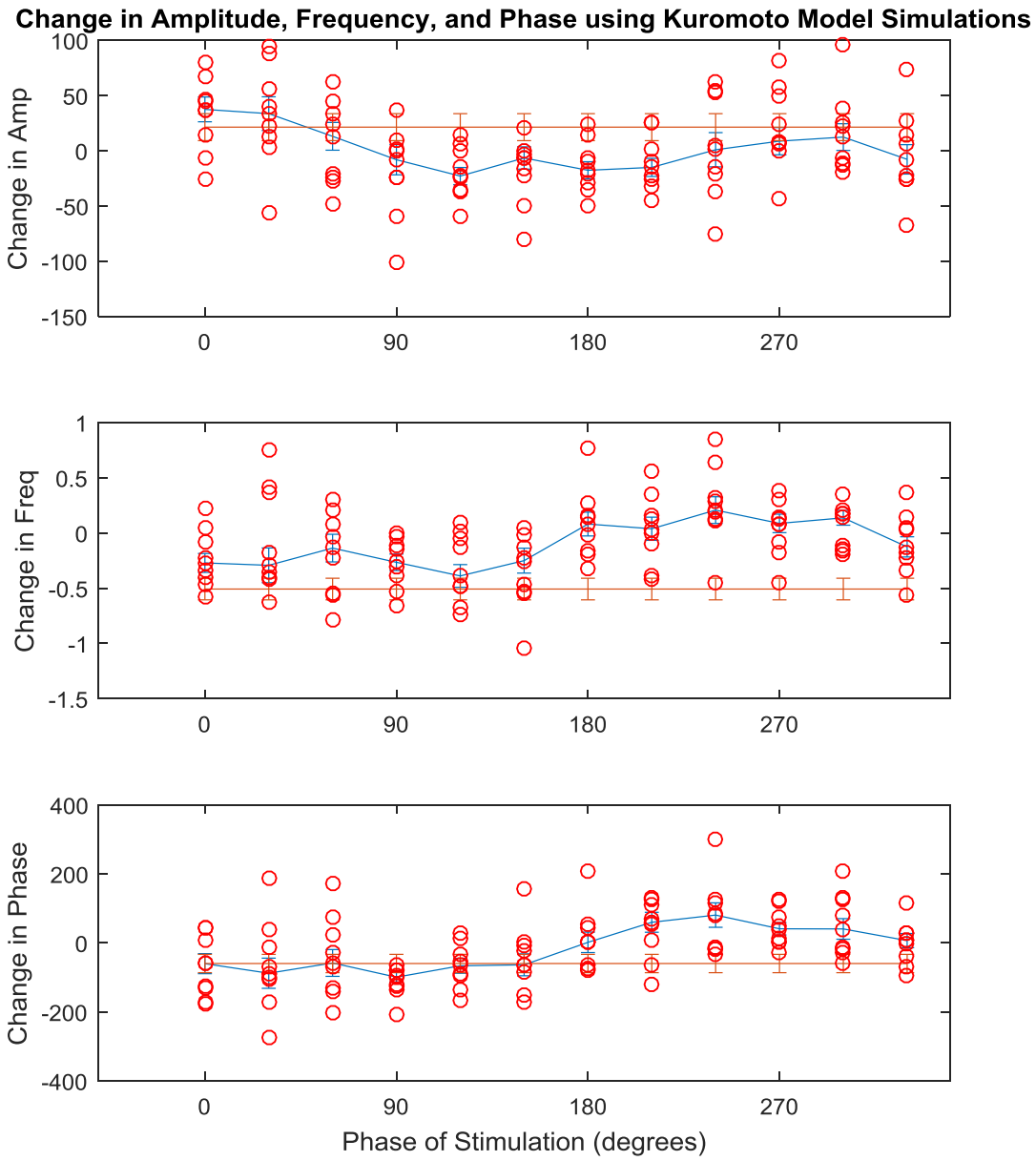

Figure 20: Change in Amplitude, Frequency, and Phase Curves of Simulated Data using Scaled, Experimental Change in Frequency Curve (Figure 19) as PRC Function

The change in amplitude (in m/s^2), Δa (1st row), frequency (in Hz), Δf (2nd row), and phase (in degrees), $\Delta\theta$ (3rd row), were calculated for all 108 simulated blocks and plotted above (red circles). Linear interpolations of the median $\Delta a, \Delta f$, and $\Delta\theta$ for each phase of stimulation were plotted (blue lines) along with the standard error. The median change in amplitude, frequency, and phase for the 9 reference blocks of no stimulation were also plotted (orange lines).

From correlation coefficients computed between median change in amplitude and the derivative approximations of the median change in frequency and phase as well as those computed among all the median metrics, high correlative effects are only observed between change in amplitude and the derivative approximations. Thus, the model still preserves the relationships among the three curves as shown earlier.

Lastly, while using this PRC function appeared to align the change in frequency and phase curves more with those of the experimental data, there was no significant correlation between any of the experimental and simulated curves using this PRC function.

Directly Using Scaled, Experimental Change in Phase Curve

The scaled linear interpolation of the experimental change in phase curve (Figure 10, 3rd row) was also used in a simulation (Figure 21).

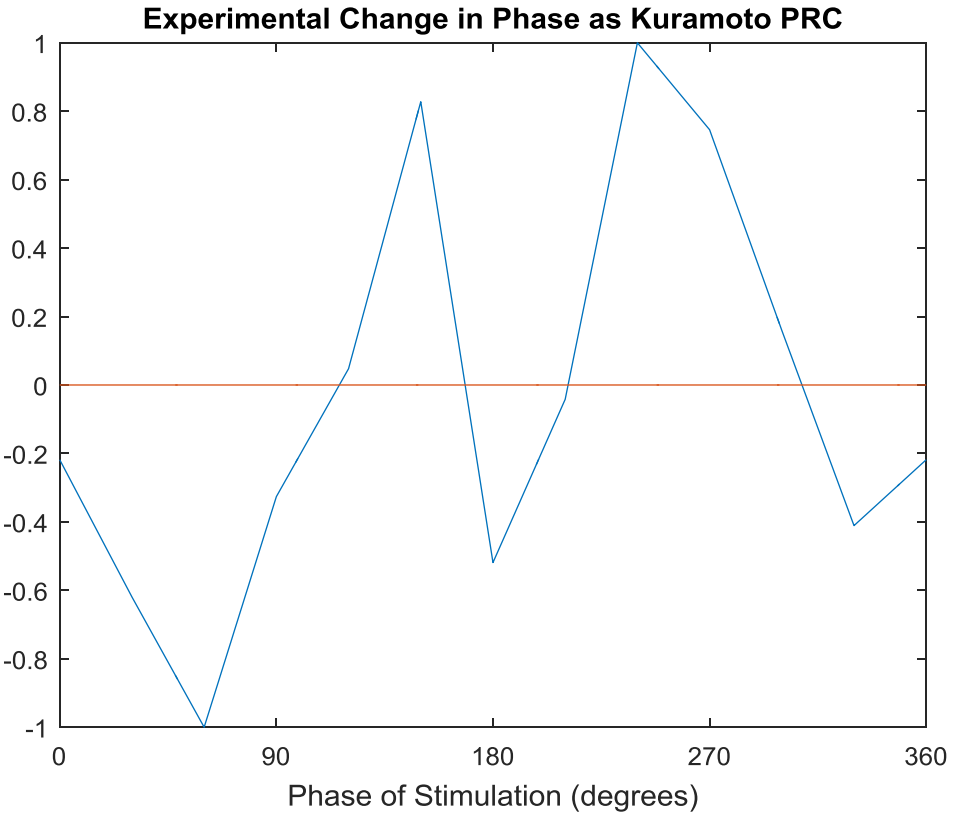

Figure 21: Scaled, Experimental Change in Phase Curve as PRC Function $z(\theta_i)$ for Extended Kuramoto Model

The linear interpolation of the change in phase curve from the experimental data (Figure 10, 3rd row) was scaled to range from $[-1, +1]$ and used as the PRC function $z(\theta_i)$ for a simulation of the extended Kuramoto model.

This simulation induced a tremor-suppressing effect at 120° (Figure 22, 1st row), in contrast to the tremor-suppressive effect at 240° observed in the experimental data (Figure 10, 1st row). Furthermore, its change in frequency and phase curves (Figure 22, 2nd and 3rd rows) are quite noisy and flat. Yet, the change in frequency curve at 120° (Figure 22, 2nd row) appears to adhere to the traditional Kuramoto model explanation of optimal tremor suppression at the positive, zero-crossing in change in phase.

Moore-Rayleigh tests demonstrate significant non-uniformity in all curves ($p < 0.05$), with the phases of the resultant vectors for $-\Delta a$, Δf, and $\Delta\theta$ are 137.7°, 226.2°, and 215.9° respectively. The latter to phases are within 10°-15° to the phases of the resultant vectors for statistical tests on the experimental change in frequency and phase curves (Table 1).

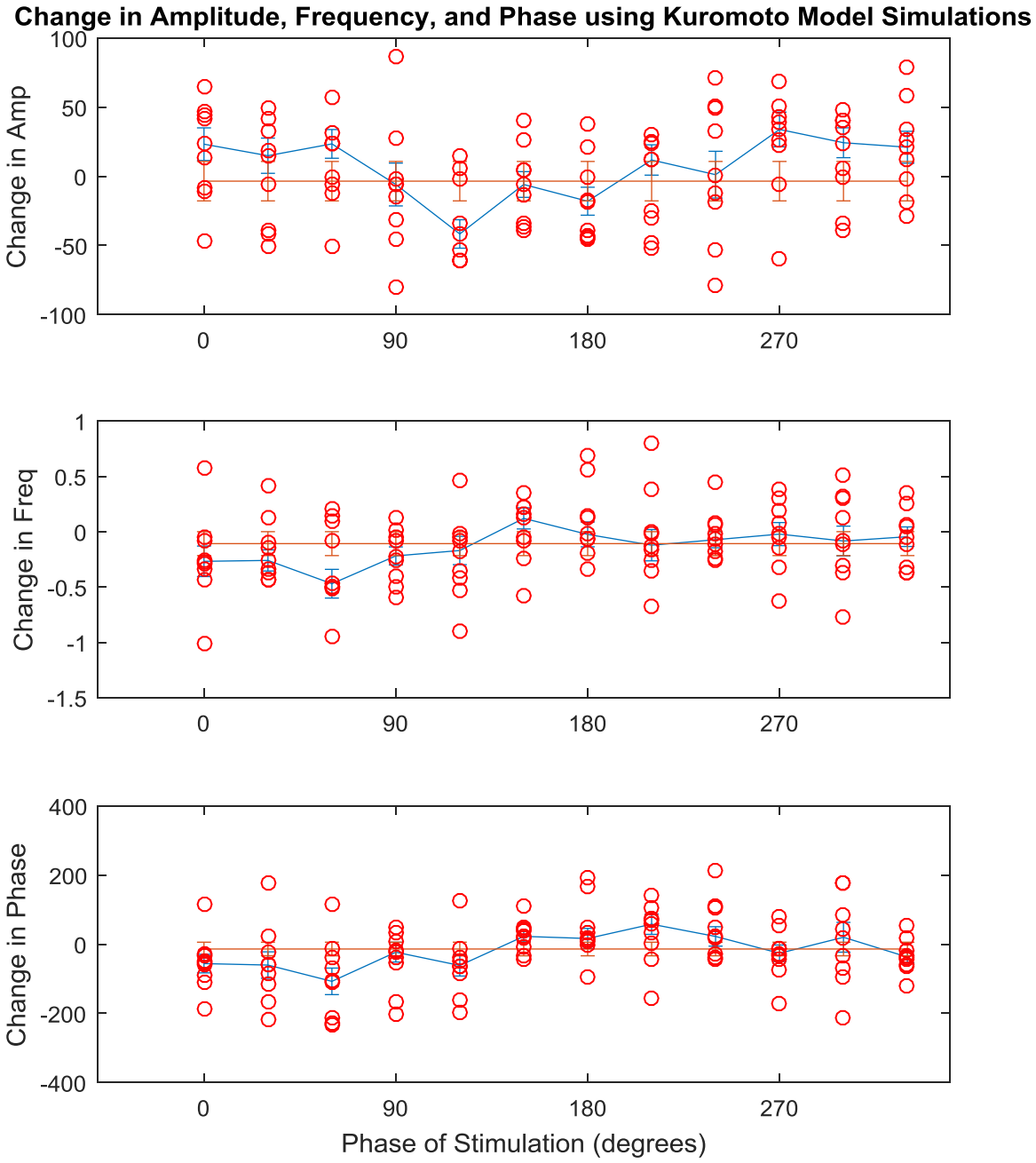

Figure 22: Change in Amplitude, Frequency, and Phase of Simulated Data using Scaled, Experimental Change in Phase Curve (Figure 21) as PRC Function

The change in amplitude (in m/s^2), Δa (1st row), frequency (in Hz), Δf (2nd row), and phase (in degrees), $\Delta\theta$ (3rd row), were calculated for all 108 simulated blocks and plotted above (red circles). Linear interpolations of the median Δa, Δf, and $\Delta\theta$ for each phase of stimulation were

plotted (blue lines) along with the standard error. The median change in amplitude, frequency, and phase for the 9 reference blocks of no stimulation were also plotted (orange lines).

For this simulation, there were no significant ($p < 0.05$) correlations between the experimental and simulated data. There were also no significant correlations between the median change in amplitude curve and the median change in frequency and phase curves or with the derivative approximations of those curves.

Discussion

This research demonstrates clinically how to find an optimal phase at which phase-locked DBS would best dampen tremor and shows computationally how a classic neural oscillator model fails to sufficiently explain the optimal strategy in an essential tremor patient. As clinical research progresses to demonstrate the effectiveness of a phase-dependent DBS strategy in a variety of patients with different tremor-related movement disorders, a corresponding theory would ideally be developed in order to describe why phase-specific DBS effectively dampens tremor. This section first summarizes this work's contributions to such an understanding and then proposes further integrated, experimental and computational work to better investigate the underlying mechanisms of phasic stimulation.

Summary of Results

In summary, there are a few key findings from this work:

- A novel paradigm for detecting and analyzing phase-dependent tremor-suppression in both experimental and simulated data was presented.
- A new, weighted circular test, the Scaled Rayleigh statistic, was outlined.
- In the essential tremor patient in which the experimental trial was conducted, significant phase-dependent tremor suppression around 240°-270° significantly correlated with large increases in frequency and phase, which are the same measure calculated using different methods and units.
- From Wilson and Moehlis, 2014, tremor suppression should correlate with the derivative of the change in frequency or phase. In this explanation, optimal stimulation would desynchronize two oscillator sub-populations at the mean population phase at which change in frequency or phase changes from negative to positive, thereby causing one sub-population to slow down and the other to speed up. However, this explanation failed to explain the direct, correlation between change in tremor amplitude and frequency/phase within the essential tremor patient.
- There is evidence of a non-linear transform between the individual oscillator PRC function used in the Kuramoto model and the oscillator population's mean change in frequency or phase. This is likely because of weakly coupled interactions among the oscillator population.

This research is the first known work to analyze the Kuramoto model's ability to simulate phase-dependent tremor suppression in comparison with clinical tremor data.

Future Work

Quantify Significant, Phase-Specific Tremor Modulation

In the single essential tremor patient in which the phasic DBS experiment was conducted, there appeared to be small dampening effect at 120°, a larger suppressive effect at 240°, and an amplification at 30° (Figure 10, 1st row). Yet, without reference blocks in which no DBS and/or constant 130Hz DBS was administered, the significance of these observed effects could not be tested. Provided said reference blocks, a paired t-test can be used to quantify the significance of such effects, with Bonferroni correction to correct for multiple comparisons among 12 phases.

The Moore-Rayleigh and Scaled Rayleigh statistics tested non-uniformity of experimental and simulated change in amplitude, frequency, and phase curves. However, they could not rigorously identify the phases at which there was significant tremor modulation or change in frequency/phase; the phase of the resultant vector is simply a weighted, mean phase of the data points.

Model Negative Correlation between Change in Tremor Amplitude and Frequency/Phase

While this work provided evidence that the Kuramoto model fails to explain the relationship between change in tremor amplitude and frequency/phase for a single essential tremor patient, a few further computational experiments and extensions could potentially show that the model can describe this phenomenon.

Search Model Parameter Space

While some model parameters were optimized to best match tremor characteristics in the absence of DBS, others parameters, i.e. number of oscillators (N) and DBS strength (β), were chosen *a priori*. Using the four proposed stimulation functions, these parameters, and possibly the previously optimized parameters as well, should be optimized to best match tremor characteristics of phasic DBS. This could be done by finding parameters that yield the best fit to the experimental change in amplitude, frequency, and phase curves. Such an optimization may find a set of parameters that, when coupled with one or more biologically-plausible stimulation functions, can describe the direct, negative correlation between tremor suppression and frequency amplification.

Model and Understand Multiple Tremor-Inducing Neural Populations

One of the motivations behind the presented, biologically-plausible stimulation functions was to incorporate the understanding that both the sub-thalamic nucleus (STN) and the global pallidus interna (GPi), a sub-cortical region, contribute to tremor. Typically, DBS electrodes are only implanted in one of these regions. Yet, with respect to phasic DBS, the relationship between these two regions and their effect on tremor has not been thoroughly researched. A phasic DBS primate study can be used to investigate their interactions. DBS electrodes can be implanted in

either the SPN or GPi while recording electrodes are inserted into both regions. Then, local field potentials (LFPs) in both regions can be recorded as phasic DBS is administered in a similar set-up to the one used in this work (Cagnan and Brown, 2016). DBS would likely interfere with LFP recordings; thus, recordings from short non-stimulated periods (i.e. after a short burst of phasic DBS has been administered) can be processed and used. From LFP recordings, the mean phase of both neural populations can be calculated and compared to each other as well as the tremor phase recorded by a hand-mounted accelerometer. These multi-region and multi-modal phase recordings can also be used to optimize and better understand the Kuramoto model, by seeking to replicate the non-linear transformation from the PRC function, which can be estimated by LFPs from the region in which DBS electrodes were implanted, to the change in tremor phase curve. Specific research should be focused on how change in phase curves between a neural population and hand tremor relate – are they directly correlated or is one correlated to the derivative approximation of another? – and how the Kuramoto model can simulate the relationship between a neural population and a downstream behavior like tremor.

Ideally grounded in clinical research on the effect of phasic DBS on the relationships among SPN, GPi, and hand tremor, the Kuramoto model can be extended in a few ways to better capture the interactions between SPN and GPi. First, the coupling constant, K, can be parameterized and made to vary among oscillators in an effort to model how a neural population's internal coupling (i.e. neurons within SPN) may differ from its external coupling (i.e. coupling between SPN and GPi neurons). Second, the distribution from which oscillator frequencies are sampled can be changed to a bi-modal distribution, to reflect that the neural activity of different regions may have different frequencies. The frequency characteristics of neural activity in STN and GPi can be extracted for their LFP recordings and either used directly in the model or used to initialize a parameter search optimization. Finally, the relationships among STN, GPi, and tremor can be explicitly described by designing different architectures of Kuramoto oscillator populations interacting with one another.

Extend the Model to Explicitly Incorporate Change in Frequency

The Tass, 2003 formulation of the Kuramoto model that incorporates DBS has four terms that describe an oscillator's 1. mean frequency, 2. coupled relationship with other oscillators, 3. noisiness, and 4. phase-dependent response to DBS (Equation 16). Another term, $h(\theta_i)$, could be added to explicitly capture the directly inverse relationship between change in tremor amplitude and frequency/phase. This term may need to be parameterized by not only the oscillator's current phase but also a recent history of its previous phases in order to approximate its change in phase. Then, a regularizing, mixture parameter, γ, can also be added (Equation 26) to weight how much the model explains tremor suppression using the "slope" explanation – that the optimal phase at which to stimulate is the one in which there is a positive-slope, zero-crossing change in an individual oscillator's PRC (Wilson

and Moehlis, 2014) – versus the "peak" explanation – that the optimal phase is the one in which there is a maximum peak in an individual oscillator's PRC. These explanations assume that a change in hand tremor frequency curve is similar to an individual oscillator's PRC, a simplification that this work shows is problematic and that needs to be further investigated as well (see "Non-Linear Transformation from Individual PRC to Change in Mean Phase of Oscillator Population
Non-Linear Transformation from Individual PRC to Change in Mean Phase of Oscillator Population").

$$\theta_i \leftarrow \theta_i + dt(\omega_i + Kr\sin(\psi - \theta_i)) + \alpha\mathcal{N}\left(0, \sqrt{dt}\right) + \gamma\beta z(\theta_i)u_i(t) + (1-\gamma)h(\theta_i)$$

Equation 26: Proposed Extension to Kuramoto Model's Update Rule

Develop Another Model that Incorporates Excitatory-Inhibitory Dynamics

The Kuramoto model makes several strong assumptions that may contribute to its inability to describe the experimental results observed. For instance, it assumes that spiking is relatively constant with its fixed angular frequency term, thereby eliminating the possibility of bursting neurons or neurons modulated by inhibition. If the above research directions using the Kuramoto model prove futile, another, more complex model, such as one that capture excitatory-inhibitory dynamics, may need to be developed.

Describe Phase-dependent DBS Strategy for Different Tremulous Pathologies and Patients

A major limitation of this work is the sample size of one essential tremor patient. The experimental trial was conducted in several essential and dystonic tremor patients (Cagnan and Brown, 2016). A preliminary analysis of the experimental data from other patients suggests that different patients may have different optimal phasic DBS strategies: the change in frequency/phase curves of a few patients seem to fit the "slope" explanation while those of other patients seem to be more consistent with the "peak" explanation observed in this work's analysis of tremors from a single essential tremor patient. Due to time constraints, multi-patient analysis was not able to be adequately conducted and included in this work. Further clinical research should include multiple patients with a variety of tremor-inducing disorders, while future computational work should be done in close collaboration with experimental work so as to be able to model different kinds of phase-dependent, tremor-suppressing effects that may vary by patient and/or pathology.

If such a biologically-consistent model were to be developed, if even for one specific movement disorder, it could then be used to identify new optimal phase-dependent DBS strategies. For example, a parameter search could be conducted to find the smallest DBS strength parameter, lowest DBS frequency, and/or the shortest duration of phasic DBS administration that could still yield effective tremor suppression. In this work, these parameters were set *a priori* as follows: DBS

strength ($\beta = 0.05$), DBS frequency (130 Hz), duration of BDS (35 ms – this corresponded to 6 pulses at 130 Hz).

Conclusion

This research was the first known work of its kind in its dual, interdisciplinary mission to identify an experimentally optimal tremor phase-locked DBS strategy in a single essential tremor patient as well as to explain computationally how phasic DBS might desynchronize a neural population and thus dampen tremor. While a coherent, underlying mechanism that can comprehensively explain the tremor-suppressing effects of phasic DBS in the tested essential tremor patient is still unknown, this work nonetheless made contributions to this goal as well as to the fields of statistics and computational neuroscience, by presenting a new, weighted circular statistic, the scaled Rayleigh test, implementing more biologically-plausible stimulation functions to be used in the Kuramoto model, and highlighting several shortcomings of the model. Finally, this dissertation proposes future directions of research that contribute to the growing body of work to develop energy-efficient yet effective closed-loop DBS therapies.

This work would not have been possible without the support and collaboration of Professor Rafal Bogacz, Dr. Hayriye Cagnan, and Dr. Gihan Weerasinghe.

References

1002072 C (2016a) Family of Rayleigh Statistics Toolbox. Available at: http://uk.mathworks.com/matlabcentral/fileexchange/56485-family-of-rayleigh-statistics-toolbox.

1002072 C (2016b) Kuramoto Model Simulation. Available at: http://bit.ly/kuramoto_sim [Accessed March 31, 2016].

1002072 C (2016c) Modelling Neurons as Kuramoto Oscillators. Available at: http://bit.ly/kuramoto_tutorial [Accessed March 31, 2016].

Azodi-Avval R, Gharabaghi A (2015) Phase-dependent modulation as a novel approach for therapeutic brain stimulation. Front Comput Neurosci 9:26 Available at: http://journal.frontiersin.org/article/10.3389/fncom.2015.00026/abstract.

Baizabal-Carvallo JF, Kagnoff MN, Jimenez-Shahed J, Fekete R, Jankovic J (2014) The safety and efficacy of thalamic deep brain stimulation in essential tremor: 10 years and beyond. J Neurol Neurosurg Psychiatry 85:567–572 Available at: http://jnnp.bmj.com.libproxy.ucl.ac.uk/content/85/5/567.

Benabid AL, Pollak P, Hoffmann D, Gervason C, Hommel M, Perret JE, de Rougemont J, Gao DM (1991) Long-term suppression of tremor by chronic stimulation of the ventral intermediate thalamic nucleus. Lancet 337:403–406.

Berens P (2012) Circular Statistics Toolbox (Directional Statistics). Available at: http://www.mathworks.com/matlabcentral/fileexchange/10676-circular-statistics-toolbox--directional-statistics- [Accessed March 31, 2016].

Best EN (1979) Null space in the Hodgkin-Huxley Equations. A critical test. Biophys J 27:87–104.

Beudel M, Brown P (2015) Adaptive deep brain stimulation in Parkinson's disease. Parkinsonism Relat Disord 22:1–4 Available at: http://dx.doi.org/10.1016/j.parkreldis.2015.09.028.

Butterworth S (1930) On the theory of filter amplifiers. Exp Wirel Wirel Eng 7:536–541.

Cagnan H, Brittain J, Little S, Foltynie T, Limousin P, Zrinzo L, Hariz M, Joint C, Fitzgerald J, Green AL, Aziz T, Brown P (2013) Phase dependent modulation of tremor amplitude in essential tremor through thalamic stimulation.

Cagnan H, Brown P (2016) Tremor Supression via Phase Tracked Deep Brain Stimulation in Essential and Dystonic Tremor Patients (in submission).

Chen CC, Brucke C, Kempf F, Kupsch A, Lu CS, Lee ST, Tisch S, Limousin P, Hariz M, Brown P (2006) Deep brain stimulation of the subthalamic nucleus: a two-edged sword. CurrBiol 16:R952–R953 Available at: http://www.sciencedirect.com/science/article/pii/S0960982206023487.

Guttman R, Lewis S, Rinzel J (1980) Control of repetitive firing in squid axon

membrane as a model for a neuroneoscillator. J Physiol 305:377–395 Available at: http://scholar.google.com/scholar?hl=en&btnG=Search&q=intitle:Control+of+repetitive+firing+in+squid+axon+membrane+as+a+model+for+a+neuron+oscillator#0\nhttp://jp.physoc.org/content/305/1/377.short\nhttp://www.pubmedcentral.nih.gov/articlerender.fcgi?artid.

Hammond C, Bergman H, Brown P (2007) Pathological synchronization in Parkinson's disease: networks, models and treatments. Trends Neurosci 30:357–364.

Hirschmann J, Özkurt TE, Butz M, Homburger M, Elben S, Hartmann CJ, Vesper J, Wojtecki L, Schnitzler A (2013) Differential modulation of STN-cortical and cortico-muscular coherence by movement and levodopa in Parkinson's disease. Neuroimage 68:203–213 Available at: http://dx.doi.org/10.1016/j.neuroimage.2012.11.036.

Hua SE (2004) Posture-Related Oscillations in Human Cerebellar Thalamus in Essential Tremor Are Enabled by Voluntary Motor Circuits. J Neurophysiol 93:117–127 Available at: http://jn.physiology.org/cgi/doi/10.1152/jn.00527.2004.

Kuramoto Y (1984) Chemical oscillations, waves and turbulence.

Little S, Beudel M, Zrinzo L, Foltynie T, Limousin P, Hariz M, Neal S, Cheeran B, Cagnan H, Gratwicke J, Aziz TZ, Pogosyan A, Brown P (2015) Bilateral adaptive deep brain stimulation is effective in Parkinson's disease. J Neurol Neurosurg Psychiatry:jnnp – 2015–310972 Available at: http://jnnp.bmj.com/lookup/doi/10.1136/jnnp-2015-310972.

Little S, Brown P (2012) What brain signals are suitable for feedback controzl of deep brain stimulation in Parkinson's disease? Ann N Y Acad Sci 1265:9–24.

Little S, Pogosyan A, Neal S, Zavala B, Zrinzo L, Hariz M, Foltynie T, Limousin P, Ashkan K, Fitzgerald J, Green AL, Aziz TZ, Brown P (2013) Adaptive deep brain stimulation in advanced Parkinson disease. Ann Neurol:449–457.

Mardia K (1975) Statistics of Directional Data. J R Stat Soc Ser B-Methodological 37:349–393 Available at: http://www.jstor.org/stable/2984782\npapers2://publication/uuid/996E21B4-6B48-4666-B2C5-5D89C94577C3.

Moore BYBR (1980) A modification of the Rayleigh test for vector. 67:175–180.

Netoff T, Schwemmer MA, Lewis TJ (2012) Experimentally Estimating Phase Response Curves of Neurons : Theoretical and Practical Issues. In: PRCs in Neuroscience; Theory, Experiment and Analysis, pp 95–130.

Ray NJ, Jenkinson N, Brittain J, Holland P, Joint C, Nandi D, Bain PG, Yousif N, Green A, Stein JS, Aziz TZ (2009) The role of the subthalamic nucleus in response inhibition: Evidence from deep brain stimulation for Parkinson's disease.

Neuropsychologia 47:2828–2834.

Rosa M, Arlotti M, Ardolino G, Cogiamanian F, Marceglia S, Di Fonzo A, Cortese F, Rampini PM, Priori A (2015) Adaptive deep brain stimulation in a freely moving parkinsonian patient. Mov Disord 30:2014–2016.

Tass PA (2003) A model of desynchronizing deep brain stimulation with a demand-controlled coordinated reset of neural subpopulations. 88:81–88.

Wilson D, Moehlis J (2014) Optimal Chaotic Desynchronization for Neural Populations. 13:276–305.

Wilson D, Moehlis J (2015) Determining individual phase response curves from aggregate population data. 022902:1–10.

Zar JH (2010) Biostatistical Analysis.

Zhang K, Bhatia S, Oh MY, Cohen D, Angle C, Whiting D (2010) Long-term results of thalamic deep brain stimulation for essential tremor. J Neurosurg 112:1271–1276.

Appendix 1: Alternative Metrics of Evaluating Effects of Tremor Suppression

Alternative metrics were developed for calculating change in amplitude, frequency, and phase. A summary of them will be presented followed by an explanation of each metric.

Change in Amplitude

The results reported in this dissertation use the change in amplitude metric given by Equation 4. However, 10 alternative metrics were developed. The p-values and phases of their result vectors from the Moore-Rayleigh and Scaled Rayleigh tests are provided in Table 9.

The mean phase of the result vector for all tests for which the $p < 0.05$ threshold was met (bolded in Table 9) was 69.8°, with a standard deviation of 8.7°. This is the diametric opposite of 249.8°.

	p-value		Phase of resultant vector	
	Moore-Rayleigh	*Scaled Rayleigh*	*Moore-Rayleigh*	*Scaled Rayleigh*
'subtract_last_block'	**0.0137**	**0.0277**	**75.1°**	**82.8°**
'subtract_last_block_norm'	**0.0165**	0.9239	**73.4°**	147.5°
'point_normalize'	0.205	0.7449	49.0°	13.7°
'simple_median'	0.4424	0.4246	103.7°	117.1°
'normalize'	0.2393	0.0521	64.1°	359.6°
'subtract_prev'	**0.0002**	**10^{-4}**	**61.5°**	**61.4°**
'subtract_prev_norm'	**10^{-4}**	0.2002	**64.4°**	24.8°
'regression'	0.6202	0.5376	143.9°	148.4°
'poly2_latent'	0.079	0.0586	109.9°	111.7°
'poly2_diff'	0.6846	0.814	101.8°	126.7°

Table 9: Statistical Significance of Alternative Metrics Measuring Change in Amplitude in Experimental Data

Tests of metrics for which the $p < 0.05$ threshold was met are bolded. Using Bonferroni correction ($\alpha = 10$), the adjusted threshold to meet is $p < 0.005$; the tests that meet the multiple comparisons threshold are underlined.

Change in Frequency & Phase

The results reported in this dissertation use the change in frequency and phase metrics given by Equation 4 and Equation 11 respectively. However, 8 alternative metrics – 2 for change in phase and 6 for change in frequency – were developed. Furthermore, there were 2 methods for calculating the frequency for a period: 1. using the median of the instantaneous frequency, and 2. estimating frequency from

the number of zero-crossings in tremor amplitude. The p-values from the Moore-Rayleigh and Scaled Rayleigh tests are provided in Table 10.

The mean phase of the result vector for all tests for which the $p < 0.05$ threshold was met (bolded in Table 9) was 267.2 °, with a standard deviation of 16.2°.

	p-value	
	Moore-Rayleigh	*Scaled Rayleigh*
'prc_point_normalize' (inst)	**0.004**	**<u>0.0026</u>**
'prc_point_normalize' (zc)	**0.0039**	**0.0146**
'prc_first_last_median'(inst)	**0.0034**	**<u>0.0016</u>**
'prc_first_last_median'(zc)	**<u>0.0026</u>**	**0.0111**
'subtract_last_block'(inst)	**0.0174**	0.1019
'subtract_last_block' (zc)	**<u>0.0002</u>**	**<u>10^{-4}</u>**
'subtract_last_block_norm'(inst)	**0.0164**	0.1112
'subtract_last_block_norm' (zc)	**<u>0.0002</u>**	**<u>0.0002</u>**
'simple_median'(inst)	0.0992	**0.0396**
'simple_median' (zc)	**0.0386**	**0.0319**
'normalize'(inst)	0.3488	0.4537
'normalize' (zc)	0.2842	0.2606
'subtract_prev'(inst)	**<u>0.0019</u>**	**<u>0.0014</u>**
'subtract_prev' (zc)	**0.004**	**0.0132**
'subtract_prev_norm'(inst)	**<u>0.0018</u>**	**<u>0.0019</u>**
'subtract_prev_norm' (zc)	**0.0036**	**0.018**

Table 10: Statistical Significance of Alternative Metrics Measuring Change in Frequency and Phase in Experimental Data

Tests of metrics for which the $p < 0.05$ threshold was met are bolded. Using Bonferroni correction ($\alpha = 16$), the adjusted threshold to meet is $p < 0.0031$; the tests that meet the multiple comparisons threshold are underlined. "inst" denotes metrics that used instantaneous frequency; "zc" denotes those that used the zero-crossing method to calculate frequency.

Alternative Metrics

'subtract_last_block'

Used for change in amplitude and frequency, this metric took the difference between the median amplitude or instantaneous frequency (or zero-crossing estimate of the frequency) over the whole 5-second period of the current block and that of the previous block. If there was no prior block, the median amplitude or frequency (or zero-crossing estimate) was calculated for the 1-second no-stimulation period immediately preceding the current 5-second block.

'subtract_last_block_norm'
Used for change in amplitude and frequency, this metric normalized the 'subtract_last_phase' metric by dividing it by the median amplitude or frequency (or zero-crossing estimate) of the previous block.

'point_normalize'
Used for change in amplitude, this metric took the difference between the amplitude at the end of the current block (t = 5s) and the amplitude at the beginning of the current block (t = 0s) and normalized this difference by the latter term.

'simple_median'
Used for change in amplitude and frequency, this metric was simply the median of the amplitude or instantaneous frequency (or zero-crossing estimate of frequency) over the whole 5-second period of the current block.

'normalize'
Used for change in amplitude and frequency, this metric took the difference between the median amplitude or instantaneous frequency (or zero-crossing estimate of frequency) of the last second of the current block (t = 4-5s) and that of the first second of the current block (t = 0-1s) and normalized this difference by the latter term.

'subtract_prev'
Used for change in amplitude and frequency, this metric took the difference between the median amplitude or instantaneous frequency (or zero-crossing estimate of frequency) of the whole 5-second period of the current block and that of the 1-second, no-stimulation period immediately preceding it.

'subtract_prev_norm'
Used for change in amplitude and frequency, this metric normalized the 'subtract_prev' metric by dividing it by the median amplitude or instantaneous frequency (or zero-crossing estimate of frequency) of the 1-second, no-stimulation period immediately preceding it.

'regression'
Used for change in amplitude, this metric was the slope of a line fitted to the tremor amplitude values for the whole 5-second period of the current block.

'poly2_latent'
Used for change in amplitude, this metric was the time step at which a quadratic line fit to the tremor amplitude values for the whole 5-second period of the current block was a minimum or maximum point.

'poly2_diff'
Used for change in amplitude, this metric was the difference between the minimum or maximum point from a fitted quadratic line to the tremor amplitude values for the whole 5-second period of the current block and the midpoint value between the tremor amplitude values at the beginning (t = 0s) and end (t = 5s) of the block.

'prc_point_normalize'

Used for change in phase, this metric took the difference between the unwrapped phase at the end of the 5-second period of the current block (t = 5s) and the projected, unwrapped phase based on the median frequency (or zero-crossing estimate) of the previous block and normalized it by time (5 seconds) and by the length of a cycle (2π). If there was no previous block, the 1-second, no-stimulation period immediately preceding the current block was used as the reference signal instead. The only difference between this metric and the one used in this dissertation was the reference frequency; for the default change in phase metric, the reference frequency was the median instantaneous frequency of the 1-second, no-stimulation period immediately preceding the current block.

'prc_first_last_median'

Used for change in phase, this metric is similar to the previous metric, except it used the median unwrapped phase of the last 100ms second of the current block (t = 4.9-5s) and the projected, unwrapped phase of the same 100ms period using the previous block's frequency as the reference frequency.

Appendix 2: Simulated Change in Phase Curves with Different Numbers of Oscillators

Figure 23 shows how the oscillator population's change in phase curve diverges more from the individual PRC function, $z(\theta_i) = \cos(\theta_i + \frac{\pi}{6})$, as the number of oscillators increases.

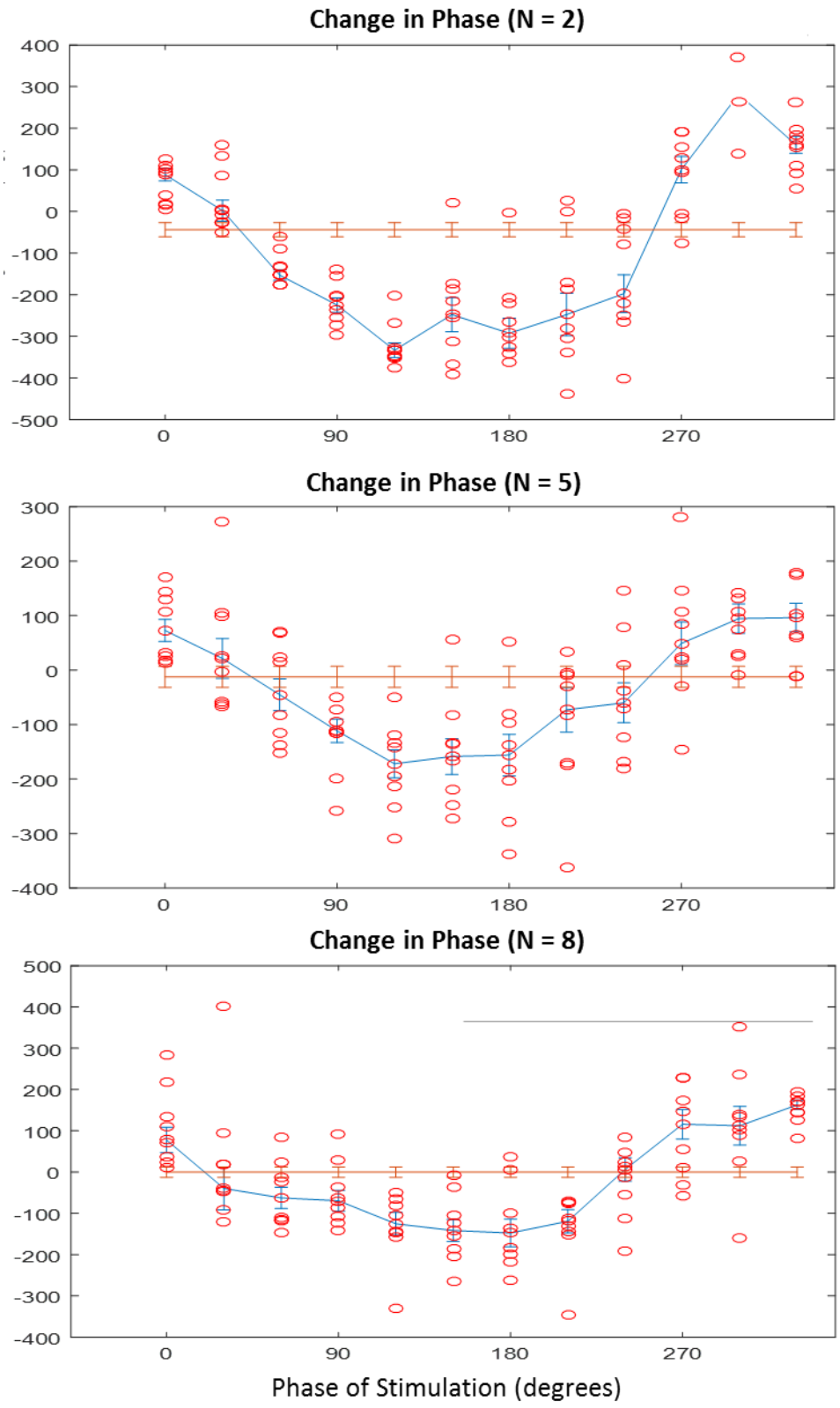

Figure 23: Change in Phase Curve for Simulated Data when Different Numbers of Oscillators (N = 2, 5, 8)

The change in phase, $\Delta\theta$, was calculated for all 108 simulated blocks generated in each simulation using the 2 oscillators (1st row), 5 oscillators (2nd row), and 8 oscillators (3rd row) respectively and plotted above (red circles). When using N = 2, 5, and 8 oscillators, linear interpolations of the median $\Delta\theta$ for each phase of stimulation are plotted (blue lines) along with the standard error. The median change in phase values for the 9 reference blocks of no stimulation are also plotted (orange lines).

Appendix 3: Different Stimulation Functions

The change in frequency (Figure 24) and phase curves (Figure 25) for simulations using the “half”, “random”, and “uniform” stimulation functions are included here.

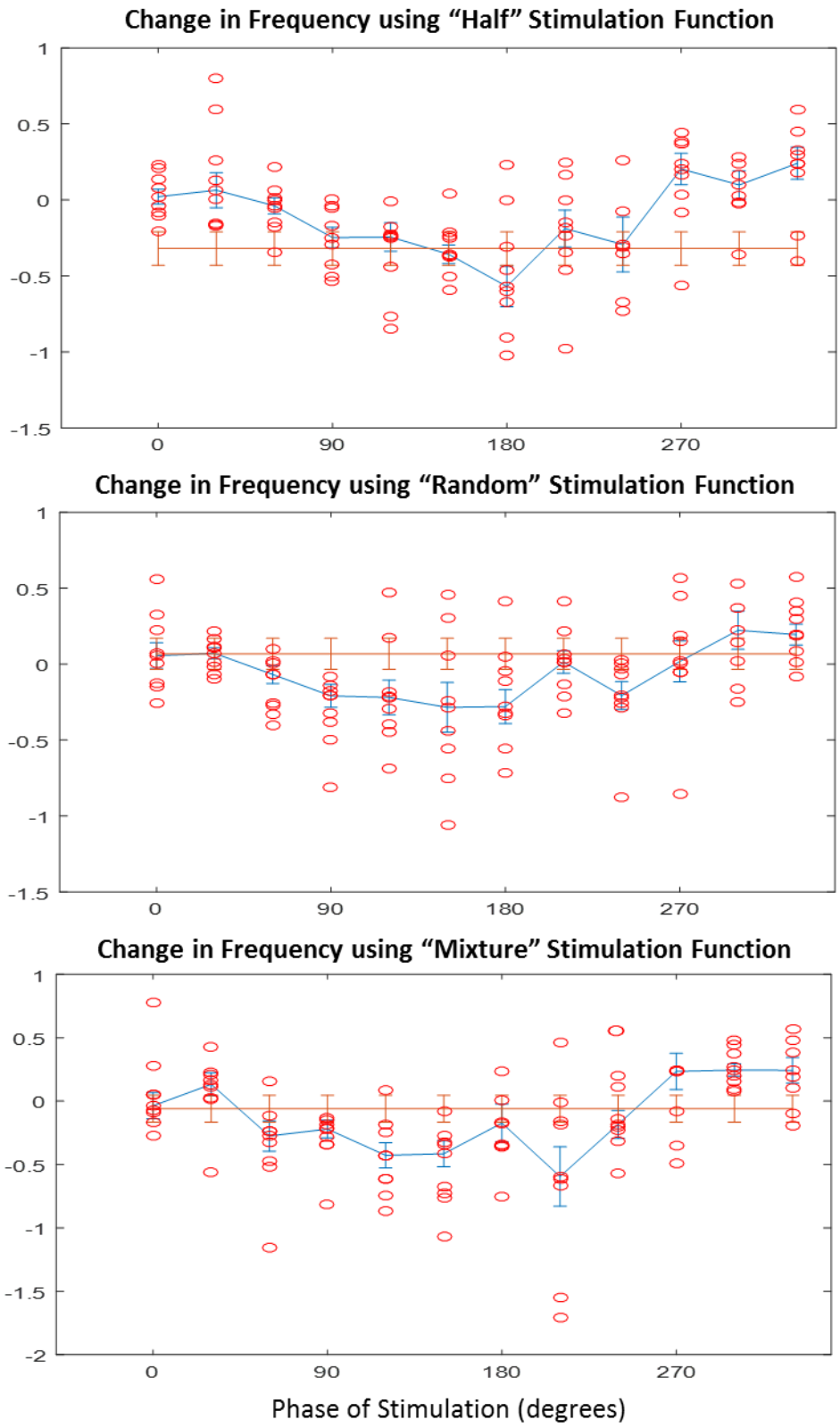

Figure 24: Change in Frequency Curves for Simulated Data when using “Half”, “Random”, and “Mixture” Stimulation functions

The change in frequency, Δf, was calculated for all 108 simulated blocks generated in each simulation using the "Half" (1st row), "Random" (2nd row), and "Mixture" (3rd row) stimulation function and plotted above (red circles). When using each of these stimulation functions, linear interpolations of the median Δf for each phase of stimulation are plotted (blue lines) along with the standard error. The median change in frequency values for the 9 reference blocks of no stimulation are also plotted (orange lines).

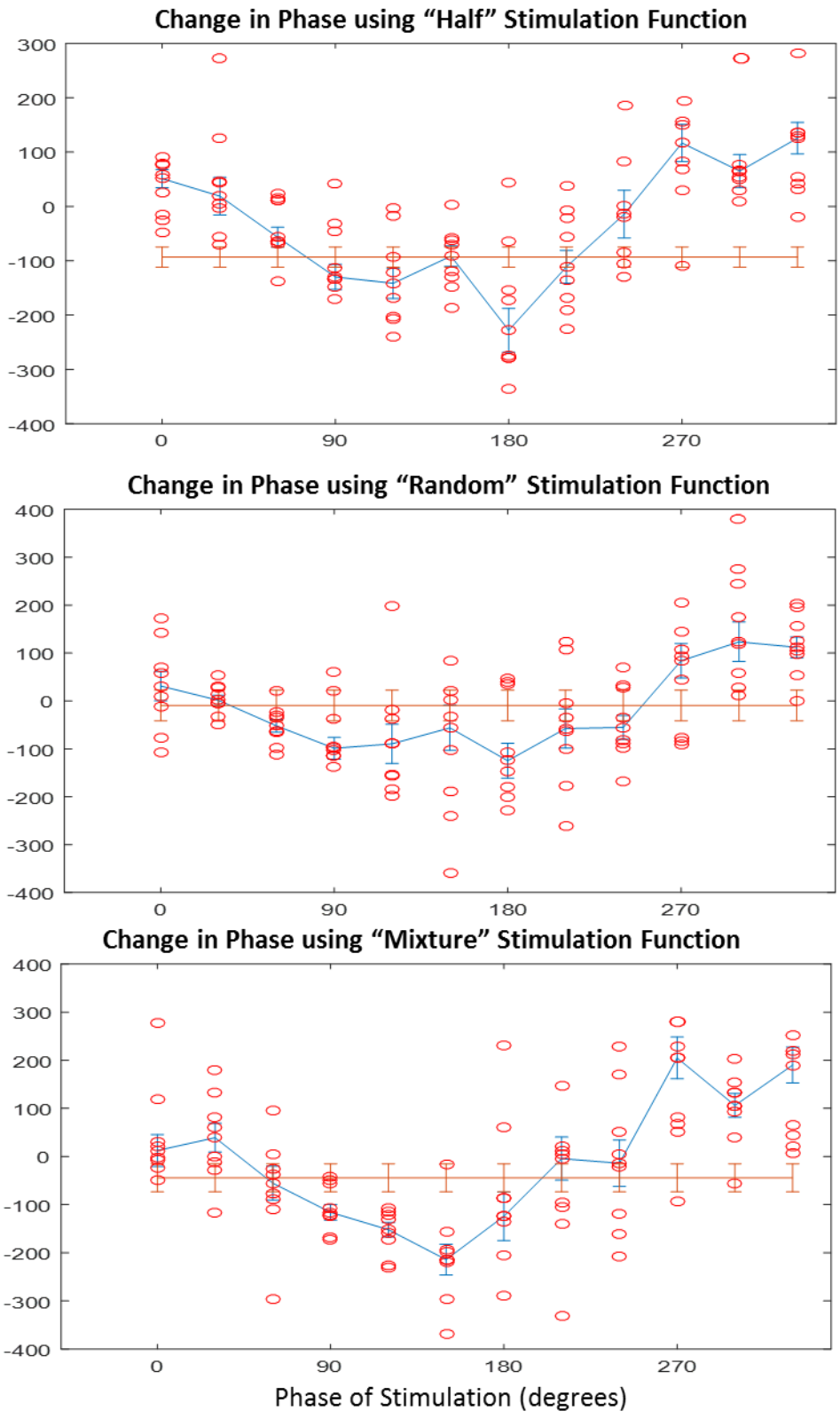

Figure 25: Change in Phase Curves for Simulated Data when using “Half”, “Random”, and “Mixture” Stimulation functions

The change in phase, $\Delta\theta$, was calculated for all 108 simulated blocks generated in each simulation using the "Half" (1st row), "Random" (2nd row), and "Mixture" (3rd row) stimulation function and plotted above (red circles). When using each of these stimulation functions, linear interpolations of the median $\Delta\theta$ for each phase of stimulation are plotted (blue lines) along with the standard error. The median change in phase values for the 9 reference blocks of no stimulation are also plotted (orange lines).

Appendix 4: Extended Kuramoto Model Simulation Tool

A web simulation of the Kuramoto neural oscillators was developed to be used in a public engagement event with local Oxfordshire high school students. It can be used as a game, in which users earn points by desynchronizing a population of Kuramoto neural oscillators, to intuitively teach the optimal phase-dependent DBS strategy that the Kuramoto model suggests (i.e. stimulating at the positive zero-crossing in the PRC function). It can also be used as a research and visualization tool, where nearly all the Kuramoto simulation parameters can be set by the user, including a phasic stimulation strategy. The user can then observe the state of the neural oscillator population, its synchrony, and the tremor signal as the simulation runs with the user-specified model parameters.

The simulation tool can be accessed at this link: http://bit.ly/kuramoto_sim.

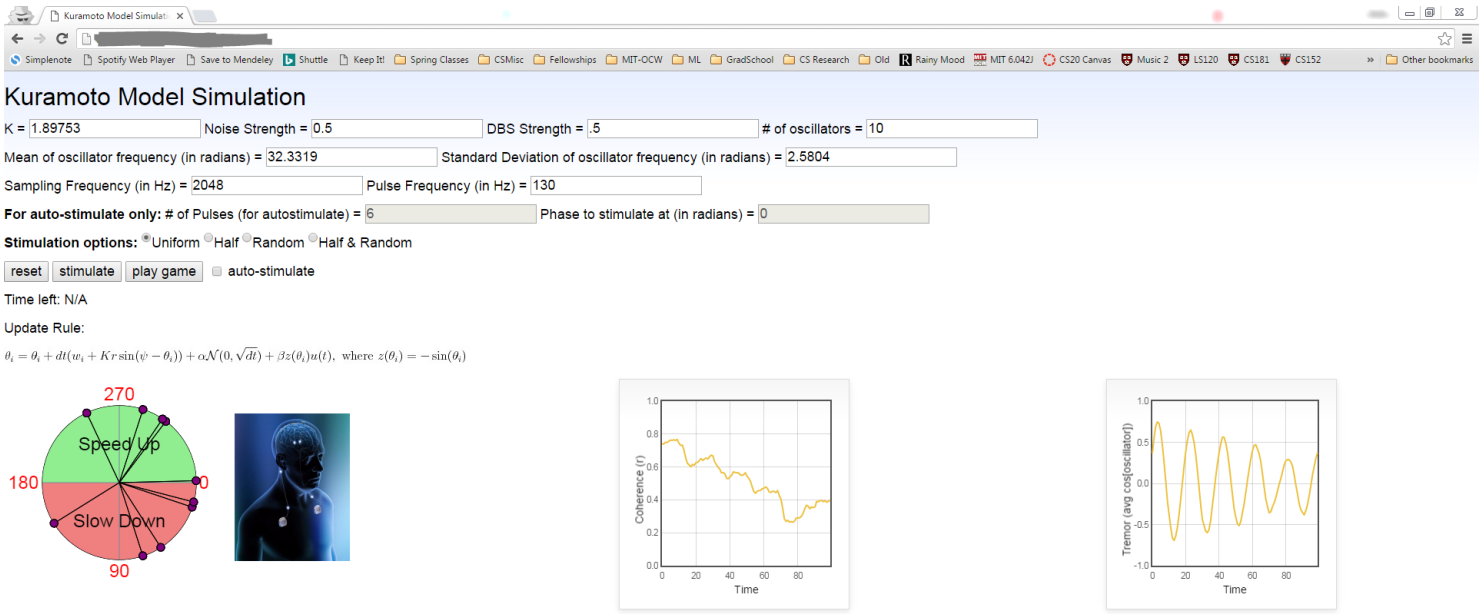

Figure 26: Screenshot of Simulation Tool